Engineering and Technology Journal
Journal homepage: https://etj.uotechnology.edu.iq

Utilizing remote sensing and aerogeophysical data for spatial decision support system for optimal gold mineralization site identification in North-Central Nigeria

Abdullahi S. , Ejepu J.S. *

Department of Geology, School of Physical Sciences, Federal University of Technology Minna, Niger State, Nigeria.
*Corresponding author Email: ejepu.jude@futminna.edu.ng

HIGHLIGHTS

- Remote sensing is employed to detect potential gold reserves in the study.
- The research facilitates comprehension of structural geology and its mapping.
- FOPCA and aeromagnetic techniques are utilized for advanced interpretation.
- GIS modeling enhances the understanding of zones with mineral prospects.

ARTICLE INFO

Handling editor: Imzahim A. Alwan

Keywords:

Gold mineralization

Hydrothermal alteration

Mineral-prospective zones

Analytic Hierarchy Process

Fuzzy Overlay

ABSTRACT

This study presents a comprehensive investigation utilizing remote sensing data and aerogeophysical datasets to identify potential economic gold mineralization sites in Zungeru, North-Central Nigeria. The research objectives include understanding the structural setting, mapping lithologic contacts, and detecting hydrothermally altered zones. Spatial suitability analysis was conducted on processed datasets. Feature-Oriented Principal Component Analysis (Crosta approach) was applied to selected Landsat 8 OLI imagery bands for mapping hydroxyl and iron oxide alterations. Additionally, regional topographic lineaments were mapped using SRTM DEM, and subsurface lineaments were identified using aeromagnetic data. Interpretation of the aeromagnetic data revealed complex anomalies associated with various structural characteristics, such as faults, folds, and fractures. The investigation of hydrothermal alteration zones through gamma-ray spectrometry data and K/eTh ratio analysis demonstrated a significant connection with igneous intrusions, further supported by ternary maps of the radioelements. Five thematic maps representing factors that control gold mineralization were integrated using GIS modeling to identify prospective zones. Five distinct mineral-prospective zones are delineated, showing varying levels of mineralization potential. The "Very Good" to "Good" zones are predominantly aligned in the NNE direction, with some occurrence in the NW quadrant. The spatial correlation with lithological characteristics and lineament features suggests their strong influence on mineral prospectivity. Around 76% of gold mineralization is within the most favorably projected zones. Both models show considerable reliability, with predictive accuracies surpassing 70%, as validated using the ROC/AUC metric. The Fuzzy Logic model showcases the highest predictive efficacy, with a prediction level of 78.3%. The validation results of gold mining sites from the models indicate a percentage agreement of 75%. The study guides future exploration efforts, directing them toward areas with the highest promise of finding gold. This work is instrumental in optimizing resource allocation and maximizing the efficiency of exploration endeavors, paving the way for more targeted and successful gold prospecting in the region.

1. Introduction

In Nigeria, quartz veins and pegmatites within the Basement Complex rocks are often associated with gold mineralization and gemstone formation. These economic resources might be discovered as veins or as alluvial deposits. Most primary gold mineralization within the schist belt is linked with distinct lithologies of quartz veins. Mineral deposits in each area are tightly correlated with structural elements, including faults, shear zones, and variations in lithological boundaries. Therefore,

http://doi.org/10.30684/etj.2024.146400.1681
Received 27 January 2024; Received in revised form 27 March 2024; Accepted 07 April 2024; Available online 19 May 2024
2412-0758/University of Technology-Iraq, Baghdad, Iraq

successful mineral exploration requires a comprehensive understanding of the interrelationships between these structural elements and lithologic units [1].

Numerous studies have shown that geological remote sensing techniques may effectively locate and characterize mineral associations based on spectral irregularities [2-6]. Multispectral remote sensing, using imaging systems such as NASA Landsat, has been widely used in regional mineral prospecting since the 1970s. Researchers can find outflows from hydrothermal systems by studying the spectral fingerprints of minerals and their assemblages, which hydrothermal modifications alter. This method substantially facilitates the identification of mineralized zones [7-9]. Remote sensors measure the sun's electromagnetic radiation interacting with materials, allowing the determination of their spectral patterns. These spectral signatures, often referred to as "material fingerprints," enable the differentiation of similar minerals and the determination of their compositions [10].

Various methodologies and analytical methods have been implemented for processing satellite data and detecting hydrothermal alteration zones [11-15]. Hydrothermal mineral deposits are closely associated with structurally regulated mineralization, often surrounded by distinct hydrothermal wall rock alteration assemblages that may exhibit zoning [16-18]. Because of the vast range of mineral groups available, such as iron oxides, clays, and carbonates, which display diverse spectrum features, most remote sensing investigations have prioritized the analysis of hydrothermal systems [19]. Wamba et al. [20] utilized Landsat-8 and ASTER satellite imagery to successfully detect hydrothermal alteration zones associated with gold mineralization in the Ngoura-Colomines region, Eastern Cameroon, overcoming constraints posed by climatic conditions and vegetation in tropical and subtropical regions while identifying high-potential prospects for new gold prospective zones in the study area. Additionally, Shebi et al. [21] use multiscale datasets, including aeromagnetic data, ASTER, Sentinel 2, and ALOS PRISM and spectrometric gamma-ray data, integrating them for gold potentiality mapping (GPM) over the Atalla area in Central Eastern Desert, Egypt, revealing five gold-promising zones. When metal-bearing hydrothermal fluids interact with rock layers, distinctive hydrothermal alteration zones with distinct mineral complexes form [22-24]. The electromagnetic spectrum attenuation properties of these mineral occurrences may be seen in the VNIR (Visible and Near-Infrared), SWIR (Shortwave Infrared), and TIR (Thermal Infrared) spectral ranges [25, 26]. Different types of alteration, including potassic (quartz, sericite, biotite), phyllic (quartz, sericite, pyrite, muscovite, illite), argillic (quartz, kaolinite, montmorillonite, illite, muscovite), and propylitic (chlorite, carbonate calcite, epidote), are observed when hydrothermal alteration occurs in the wall rocks surrounding a mineral deposit [22]. Detecting, defining, and differentiating hydrothermal alteration is critical in mineral exploration. The alteration footprint is frequently considerably larger than the actual deposit, making it simpler to discover [23, 27, 28]. Landsat-8 satellite data have been effectively employed in identifying hydrothermal alteration minerals, specifically iron oxides, hydroxyl-bearing minerals, and carbonate-bearing minerals, on a regional scale. This has been demonstrated through several studies, including those conducted by Pour and Hashim [12], Pour et al. [29], Liu et al. [30], and Abdelnasser et al. [31].

2. Gold occurrence in Nigeria

The Nigerian Schist Belts, found in the northwest and southwest of the country, exhibit substantial gold mineralization, including alluvial, eluvial concentrations and significant vein occurrences. Notable instances are found in Maru, Anka, Malele, and other schist belt regions. These areas contain varied rock types with distinct petrographic features [32]. Previous studies compared global source rocks to Nigerian gold, linking gold origins to parent rock properties. Successful gold exploration in Nigeria's Pan-African basement requires understanding structural traits and hydrothermal mechanisms regulating gold-bearing fluid movement [33]. The primary structural controls for gold mineralization in Nigeria's Pan-African basement are structural, mainly faults and intrusives. These structural features consist primarily of faults, forming the ancient Pan-African conjugate fracture system [33]. These fault networks likely served as pathways for hydrothermal fluids, leading to gold deposits. Interestingly, regional fault structures with intense fluid interactions lack mineralization, while subsidiary structures with lower temperatures and gold solubilities host gold deposits [34]. Schist Belts, encompassing Banded Iron Formation, marble, manganese, and more, are extensively studied in Nigeria [35].

Gold mineralization relates to geological processes and alteration zones like hydrothermal activity, influencing the spectral properties of rocks and minerals. Gold exploration in Nigeria's Schist Belts, with quartz veins and pegmatites in Basement Complex rocks, remains economically crucial. Despite efforts, effective exploration faces challenges due to geological complexities and elusive alteration zones. The study was conceptualized to address the absence of a robust and data-driven spatial decision support system tailored to facilitate the identification of optimal gold mineralization sites within North-Central Nigeria. Insufficient knowledge of this has led to significant challenges in allocating resources and ineffective exploration endeavors, thus impeding the region's sustainable development trajectory. This research aims to formulate, implement, and validate an integrated spatial decision support system for gold mineral exploration. This system harnesses the fusion of remote sensing and aerogeophysical data to empower evidence-based decision-making to identify potential gold-rich sites.

3. Geological description of the study area

The research area is delineated by longitudes 6°00'00" to 6°30'00" and latitudes 9°30'00" to 10°00'00", covering approximately 3025 km² (Figure 1). This region underwent a significant orogenic event, the Pan-African orogeny, around 600 - 700 million years ago, as part of the West African Pan-African belt. This orogeny involved a continent-continent collision-type orogeny with eastward subduction, impacting the Dahomeyan basement and leading to granitic magma formation [36-38]. The research area lies within the Birnin-Gwari and Kushaka Schist Belt, characterized by metasediment-dominated belts trending

north-south, predominantly in north-western Nigeria. These Upper Proterozoic supracrustal rocks display diverse lithologies, such as clastic pelitic schists, phyllites, banded iron formations, marbles, and mafic metavolcanic, potentially containing oceanic fragments. Studies by Rahaman [39] suggest multiple depositional basins, while Oyawoye [40] and McCurry [41] propose remnants of a single cover. Olade and Elueze [42] suggested fault-controlled rift-like structures. While Grant [43], Holt [44], and Turner [45] imply varied ages based on structural and lithological associations, Ajibade et al. [46] argue for identical deformational histories in both series.

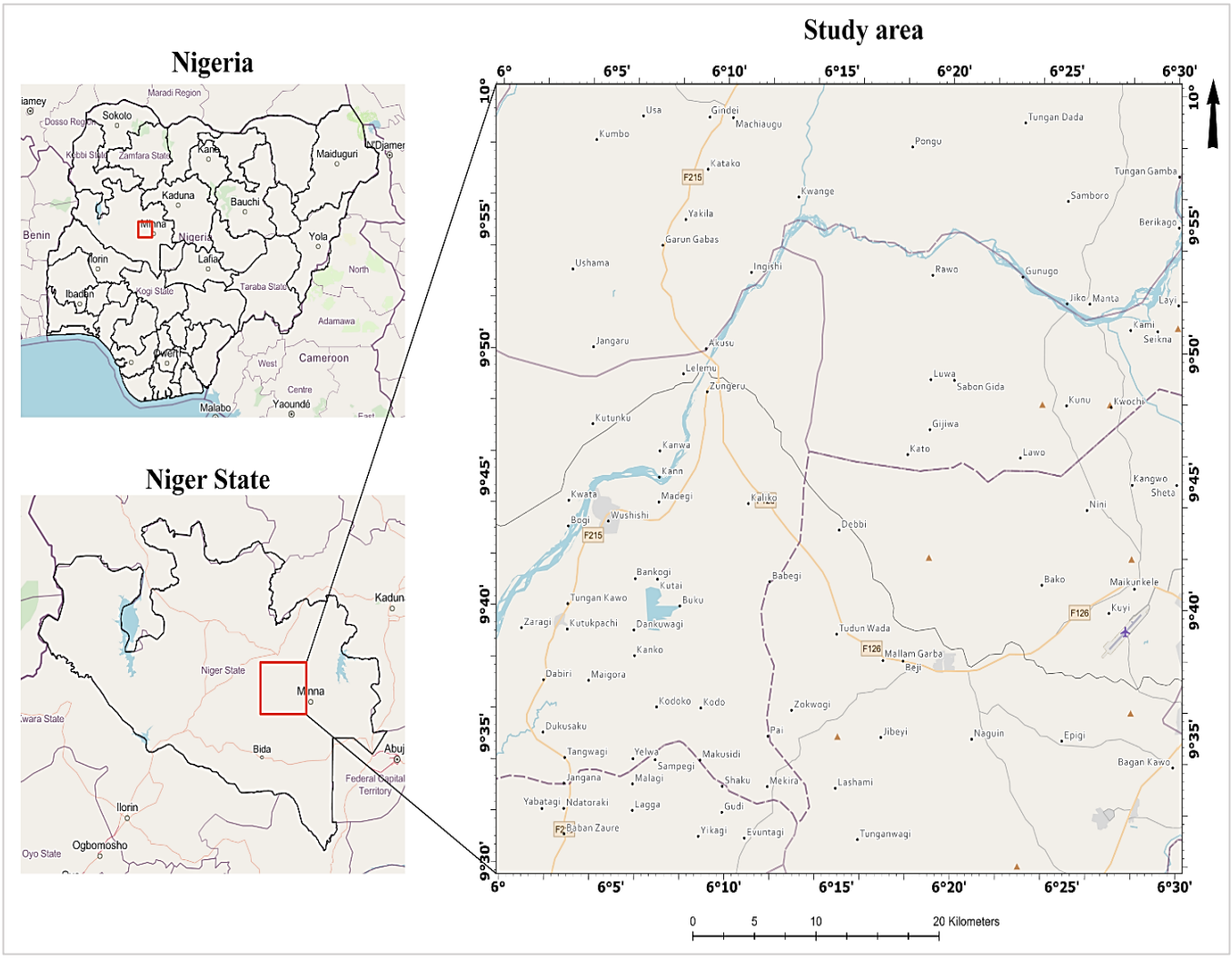

Figure 1: Location map of the study area

The relationship between schist belts and the basement is viewed by Ajibade et al. [47] as a structural break (Figure 2). The partial melting process in the upper mantle and lower crust contributed to the formation of granitic magmas and the emplacement of the Older Granites. The region then underwent an extended period of shield development until the formation of the Bida Basin during the Cretaceous period. The Zungeru-Birnin-Gwari schist formation, which displays rift-like structures governed by faults, is the dominant geological feature of the area [42,48]. The "Zungeru-Birnin Gwari schist belt" refers to the combined rocks of the Zungeru granulite formation and the Birnin-Gwari schist formation [48, 49]. According to Obaje [48], these schist belts are the remnants of larger rock formations that saw considerable intrusive action from granitic rocks. Zungeru mylonite borders the Birnin-Gwari schist formation on both sides and extends to the Kushaka schist belts' western limit [50].

The geochronology of these belts is complex, with cross-cutting Older Granites indicating an age lower limit of 750 million years. Notably, Maru Belt phyllites possess a metamorphic age of 1,040 ± 25 Ma [51]. The geochemistry of amphibolite complexes in these belts is disputed, with theories of ensialic processes [42,51] and oceanic materials [52,53]. Dominating western Nigeria, Schist Belts extend around 300 km with a north-northeast trend. Detailed studies concentrate on localities like Maru, Anka, and Zuru, linking these belts with gold mineralization. The drainage system is influenced by lithology and structural features, forming narrow river valleys along foliations and joints. The orogenic Pan-African event around 600 - 700 million years ago shaped the region's geological evolution, marked by granitic magma formation and continental collision [36-38,54].

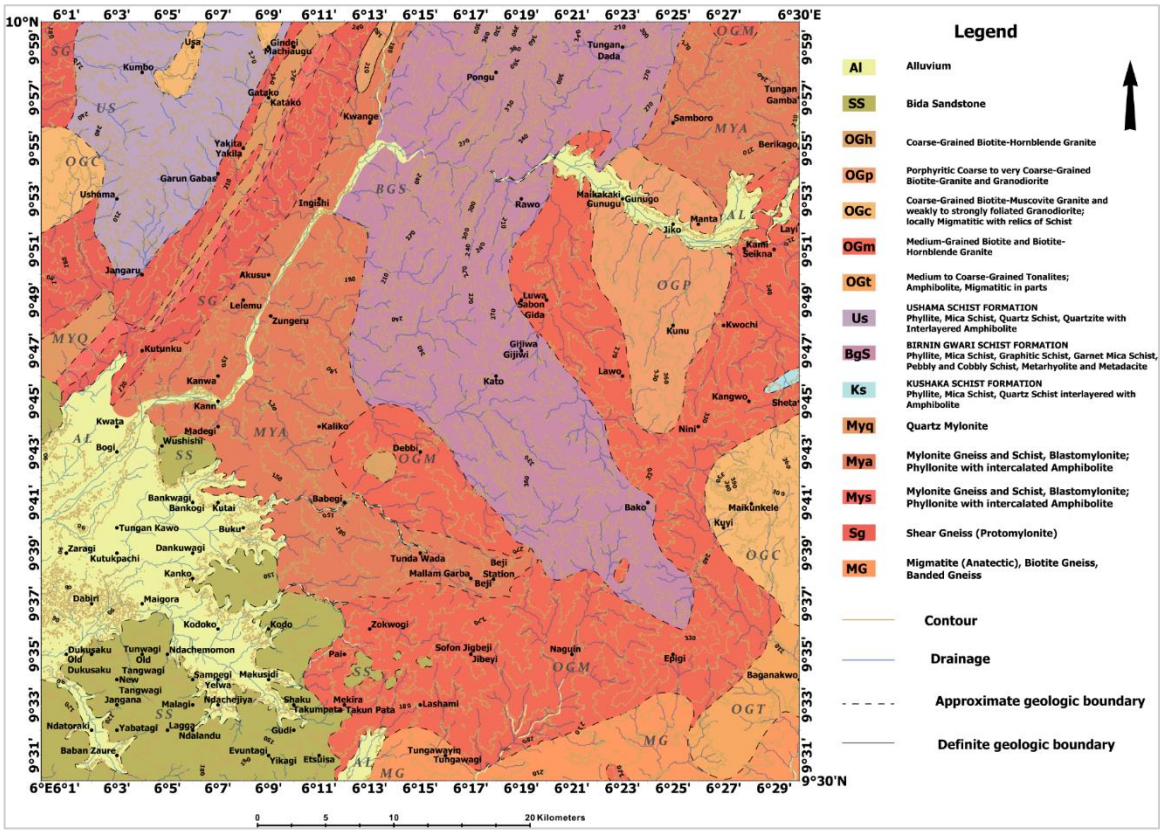

Figure 2: Geologic map of the study area

4. Methodology

4.1 Data acquisition

Launched on February 11, 2000, SRTM is an international initiative led by NIMA and NASA in partnership with DLR. It aims to acquire global elevation data and create a comprehensive, high-resolution digital Earth topographic database. SRTM employs Spaceborne Imaging Radar-C and X-Band Synthetic Aperture Radar (SIR-C and X-SAR) hardware, capturing data for a digital elevation model at a 1 arc-second interval (around 30 meters at the equator). Achieving high accuracy, both horizontally and vertically, SRTM employs radar interferometry. The 30-meter data was sourced from [55], simplifying the downloading process for elevation data from the Shuttle Radar Topography Mission website.

Part of the Landsat series, The Operational Land Imager (OLI) was launched in February 2013 aboard Landsat-8. While OLI continues the Landsat legacy of archiving moderate-resolution Earth imagery, it significantly differs from the Thematic Mapper (TM) sensors on Landsat-5 and -7. Unlike the TM's whiskbroom sensors with few detectors sweeping cross-track, OLI is a push broom sensor featuring long detector arrays that form images as the satellite moves. Unlike TMs, OLI lacks a thermal band covered by the Thermal Infrared Sensor (TIRS), which has two bands (Table 1). For this research, Landsat 8 data [56] was extracted from scene paths 189, row 053, and 190, row 053, acquired on March 15, 2022. This scene was chosen for its minimal cloud cover (about 1%) and excellent image quality (100%).

The high-resolution electromagnetic and aeroradiometric data utilized in this investigation were provided by the Nigerian Geological Survey Agency (NGSA). The aeromagnetic data survey was conducted with specific parameters, which included a flight line spacing of 500 m, tie line spacing of 2 km, and terrain clearance of 80 m. The flight direction was NW-SE, while the tie line direction followed NE-SW orientation. A high-sensitivity 256-channel airborne gamma ray spectrometer was employed using the same survey parameters for the gamma-ray spectrometric survey. The acquired data from the survey was in the form of total magnetic intensity, Potassium, equivalent Uranium, and equivalent Thorium grids.

4.2 Remote sensing data processing

Pre-processing of the downloaded Landsat 8 dataset included atmospheric correction using the Fast Line-of-Sight Atmospheric Analysis of Spectral Hypercubes (FLAASH) approach, radiometric correction, and image normalization (Figure 3). The Landsat 8 OLI imagery was pre-processed and mosaicked to create a continuous image encompassing the research region. The technique of Vegetation Suppression in ENVI 5.3 was applied to mitigate the spectral influence of vegetation within multispectral and hyperspectral imagery by utilizing data from red and near-infrared bands. This strategy enhances the interpretation of geological and urban attributes, particularly when dealing with open-canopy vegetation in imagery characterized by a moderate spatial resolution (30 m). The algorithm employs vegetation.

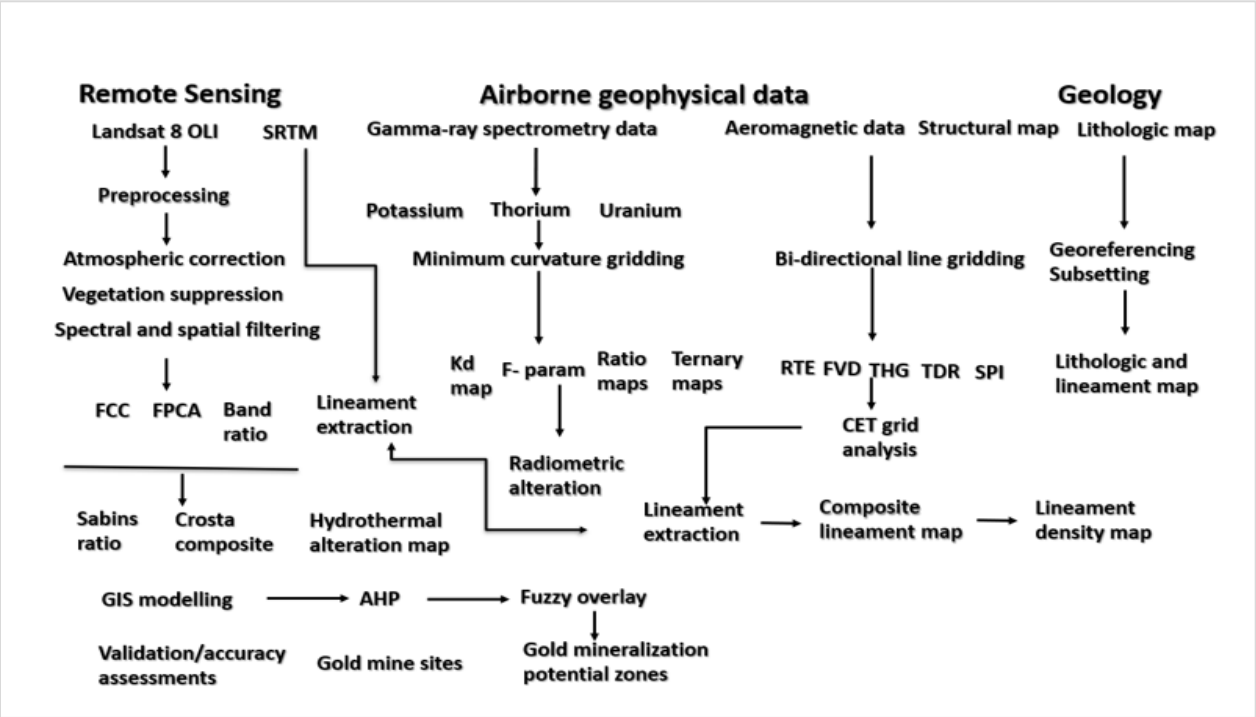

Figure 3: Research Methodology Flowchart

Transform to quantify the vegetation content within each pixel. This quantification is achieved by evaluating the correlation between each input spectral band and the presence of vegetation. Subsequently, on a per-pixel basis for each band, the vegetative constituent of the overall signal is decorrelated through the algorithm, resulting in an improved capacity to discern geologic and urban features. Using the Gram-Schmidt spectral brightening method in ENVI 5.3, the Landsat 8 VNIR (Visible Near-Infrared) and SWIR (Shortwave Infrared) bands were blended with the 15m pixel size panchromatic band 8 to improve the pixel density of the image [57-59].

Table 1: Characteristics of the various bands of Landsat 8 OLI. (Modified after) [58]

Band	Wavelength Range (µm)	Spatial Resolution (m)	Common Applications
1	0.43 - 0.45	30	Coastal studies, vegetation discrimination, soil moisture content
2	0.45 - 0.51	30	Land cover classification, soil moisture content
3	0.53 - 0.59	30	Land cover mapping, vegetation health assessment, soil type identification
4	0.64 - 0.67	30	Soil cover description, soil vs. plant discrimination, coastal studies
5	0.85 - 0.88	30	Vegetation moisture content, land surface temperature, forest fire monitoring
6	1.57 - 1.65	30	Soil moisture content, geological mapping, rock-soil separation, temperature fluctuations, humidity, presence of ferric iron, lithological modeling
7	2.11 - 2.29	30	Geological mapping, vegetation moisture content, land surface temperature, detection of hydrous minerals, lithological modeling
8	0.50 - 0.68	15	Land cover classification, coastal studies
9	1.36 - 1.38	30	Soil moisture content, geological mapping, vegetation stress detection
10	10.60 - 11.19	100	Land surface temperature, thermal mapping, urban heat island studies
11	11.50 - 12.51	100	Thermal mapping, land surface temperature, volcanic monitoring
QA	N/A	30	Quality assessment, cloud detection, atmospheric correction

4.2.1 Crosta technique hydrothermal alteration mapping

The Crosta approach, pioneered by Crosta and Moore [60], employs Principal Components (PCs) with eigenvector loadings to represent material characteristics in satellite imagery. It stands out for pinpointing target surfaces through bright/dark pixels in the main component image. Spectral bands undergo Principal Component Analysis (PCA) to capture

target features. Feature-Oriented Principal Component Selection (FPCS) assigns pixels using PCA eigenvector loadings. Crosta's method on specific bands categorizes hydrothermal alterations, including hydroxyl, iron oxide, and ferrous minerals. Composite bands 2, 4, 5, 6, and 7 are useful for mapping. PCA enhances visualization and eigenvalues for analysis. High reflectance corresponds to positive eigen loadings, and absorption is negative. Mapped changes are viewed with modified PC layers. Iron oxide (F) is green, hydroxyl (H) is red, and H+F is blue, forming a false-color composite. Altered areas are designated hydroxyl (R), iron oxides (B), and ferrous (G) for final alteration maps.

4.2.2 Surface lineament mapping

The identification of surface lineaments, which indicate the influence of underlying structural elements on local topography, was conducted using the SRTM DEM with a 30m spatial resolution. Shaded relief images of the SRTM DEM were created to emphasize the linear features, with a sun elevation angle of 30° and sun illuminating directions of 0°, 45°, 90°, 270°, and 315° perpendicular to the dominant structural orientation of the region. Using these sun-illuminating directions in extracting lineaments from DEMs is crucial as it enhances visibility, reduces noise, and aids in identifying and analyzing geological structures, such as faults and fractures, leading to a comprehensive understanding of the terrain.

The PCI Geomatica program, particularly the LINE module, automatically extracted lineaments from Landsat 8 OLI and SRTM images. RADI (filter radius), GTHR (Edge Gradient Threshold), LTHR (Curve Length Threshold), FTHR (Line Fitting Threshold), and DTHR (Linking Distance Threshold) were among the parameters used. The ideal values for these parameters that result in the desired output of extracted lineaments were carefully considered with respect to various circumstances. The lineaments were superimposed on a topographic map and a high-resolution Google satellite picture to remove spurious lineaments caused by artificial features like highways and non-geological sources. After being discovered, lineament inconsistencies were fixed, including those connected to the subset satellite imagery boundaries [61,62].

4.3 Airborne geophysical data processing

4.3.1 Aeromagnetic data

The TMI data was gridded using the least curvature approach [63,64] with a cell size of 100 m for qualitative presentation and extra-quantitative analysis. Based on the International Geomagnetic Reference Field (IGRF) of 2005, the super-regional field of 32000 nT was removed from the original TMI grid to improve its accuracy and obtain a residual grid associated with near-surface features and targets of interest.

Reduction to the Equator (RTE), filtering, and depth analysis were the three major processing techniques used to simplify and assess the subsurface structural configuration [65]. Depth analysis gave quantitative knowledge of deep magnetic anomalies, whereas RTE was used to locate and center anomalies vertically above their causative sources. Filtering techniques corroborated the anomaly's qualitative interpretation.

The First Vertical Derivative (FVD) was derived by taking the partial derivative of the magnetic data in the vertical direction (Equation 1). By magnifying high-frequency (short-wavelength) anomalies and reducing low-frequency (long-wavelength) fluctuations, this method exposes regional anomalies and aids lineament identification [66-67]. It is formulated thus:

$$\text{FVD} = \frac{\partial T}{\partial z} \tag{1}$$

The identification and improvement of subsurface structures and lithologic boundaries was aided by the transformation of the TMI grid into Total Horizontal Gradient (THG), Tilt derivative (TDR), and Analytical Signal Amplitude (ASA) grids [68 - 71].

The Total Horizontal Gradient (THG) is calculated by taking the square root of the sum of the squares of each of the 3 axis derivatives from the measured gradients (Equation 2). The equation for the horizontal gradient is:

$$\text{THG} = \sqrt{\left(\frac{\partial T}{\partial x}\right)^2 + \left(\frac{\partial T}{\partial y}\right)^2} \tag{2}$$

The first normalized edge detection method designed to address the balancing or equalizing of different amplitude edges is the tilt angle (TDR), as introduced by Miller and Singh [72]. However, this method has limitations in clearly determining the boundaries of geologic units as it tends to amplify noise in the data. The tilt angle function is derived by taking the arctangent of the ratio of the vertical derivative of the potential field to its total horizontal derivative (Equation 3).

$$TDR = \theta = tan^{-1}\left(\frac{FVD}{THG}\right) \tag{3}$$

The amplitude A of the analytic signal of the total magnetic field T is calculated from the three orthogonal derivatives of the field (Equation 4) [72].

$$|A(x,y)| = \sqrt{\left(\frac{\partial T}{\partial x}\right)^2 + \left(\frac{\partial T}{\partial y}\right)^2 + \left(\frac{\partial T}{\partial z}\right)^2} \tag{4}$$

where A = amplitude of the analytic signal, T = total magnetic field, x, y, and z = orthogonal directions.

The Source Parameter Imaging (SPI™) technique deduces magnetic depths by expanding a complex analytical signal. This method is alternatively referred to as the local wavenumber method. It encompasses a profile or grid-centered method aimed at determining magnetic source depths. Central to this approach is the intrinsic connection between source depth and the observed magnetic field's localized wavenumber (k) (Equation 5). This value can be calculated by employing horizontal and vertical gradients across each spatial point within a data grid (Equation 6).

$$D = \frac{1}{k_{max}} \tag{5}$$

$$k = \sqrt{\left(\frac{dA}{dx}\right)^2 + \left(\frac{dA}{dy}\right)^2} \tag{6}$$

4.3.2 Magnetic lineament mapping

Magnetic lineaments, represented as straight lines on maps, offer insights into lithologic links and deformation zones, emphasizing magnetic attributes. Geological processes alter bedrock's magnetic properties. Magnetite prevalence in deformation zones prompts varied magnetic changes. Metamorphism-related oxidizing fluids increase susceptibility, while magnetite deposition boosts it. Conversely, reducing metamorphic fluid intrusion reduces susceptibility. Since low-temperature weathering is supposedly the most recent chemical process in the brittle zones, assuming that most linear magnetic minima represent their surface expressions is justified. At the bedrock surface, a deformation zone may be accompanied by a topographic bedrock depression filled by soil, which may also slightly decrease the measured magnetic field. However, in some areas, several brittle zones are also related to high susceptibility. In addition to magnetic minima/maxima, a sharp discontinuity or a displacement of magnetic anomalies may indicate a potentially brittle deformation zone. A deformation zone is typically highly fractured and is characterized by concentrations of conducting minerals such as sulphides and clay [73].

Extracting lineaments was preceded by employing various enhancement techniques to process the datasets. These techniques included the utilization of Total Horizontal Gradient (THG) as depicted by Pham et al. [74] and Ekwok [75] Tilt Derivative (TDR) as described by Ejepu et al. [76], El Galladi et al. [77], the First Vertical Derivative (FVD) as implemented by Haruna et al. [78], and the application of Centre for Exploration Targeting (CET) grid analysis detailed in Holden et al. [79]. These enhancement techniques were systematically applied to the residual reduced-to-the-equator (RTE) grids.

These methodologies were systematically applied to the residual reduced-to-the-equator (RTE) grids. Notably, the THG method demonstrates reduced susceptibility to inherent dataset noise, attributed to its reliance solely on first-order horizontal derivatives of the field, as discussed by Phillips [80]. In contrast, the TDR method facilitates normalization by juxtaposing the grid's vertical and total horizontal derivatives. Furthermore, the CET grid analysis identifies density discontinuities by amalgamating texture analysis and bilateral symmetric feature detection techniques. In the context of CET operations, the standard deviation of data values at each grid location is calculated. Importantly, a conspicuously erratic computational value in relation to the underlying signal serves as an indicator of significant features [81].

4.3.3 Gamma-ray spectrometry data

The processing of the gamma-ray spectrometry data adopted the methods of Boadi et al., [82]. It has been established that mineralization zones occurring along shear zones and contacts in the Schist belt within the study area have been subject to variable degrees of hydrothermal alteration [83]. Delineation of hydrothermal alteration zones relied on regions exhibiting elevated potassium (K) concentrations extracted from gamma-ray spectrometric data, a method employed by de Quadros et al. [84]. The three radioelement concentrations—Potassium (K), equivalent uranium (eU), and equivalent thorium (eTh) were processed into ratio and ternary maps to delineate areas enriched in K, as indicated in earlier studies [84, 85]. To achieve this, a procedure was implemented to isolate heightened K values attributed to hydrothermal alteration from those related to lithology and weathering. The radiometric ternary RGB image was generated to emphasize anomalous hydrothermal alteration zones through the assignment of parameters to respective channels: (i) Red channel: Kd = (K map - Ki) / Ki, where Ki = (average K map / average eTh map) × eTh map; (ii) Green channel: F parameter = K map × (eTh map / eU map); and (iii) Blue channel: K map / eTh map ratio. Here, Ki represents the 'ideal thorium-defined potassium' value for each station with measured thorium values. Meanwhile, Kd signifies deviations (anomalies) between measured K values and calculated ideal K values (Ki). The F parameter quantifies the abundance of measured K relative to the eTh/eU ratio [85]. A K/eTh ratio map was also made to show how the resulting hydrothermally altered mineralization was distributed. The ratios of the three bands should somewhat differ on the resulting maps. These are made up of hues produced by the respective potencies of the three elements. Two color variations were produced using a histogram equalization before combining the distinct K, Th, and U histograms and K, Th, and TDR to form the composite image. The ternary maps of these images are a helpful geological and mineral exploration tool for finding zones of consistent lithology and links between diverse lithologies [86].

4.4 GIS Modelling

Integrating the Analytic Hierarchy Process (AHP) and Fuzzy Logic within the context of Multi-Criteria Decision Analysis (MCDA) in a GIS environment is a prevalent approach for assigning weights to influential factors based on their relative

importance. This approach enables a comprehensive assessment of complex decision-making scenarios by effectively capturing and quantifying the inherent uncertainties and intricacies associated with various criteria.

Saaty's [87] comparative rating scale was used for relative assessments (ranging from 1-9). Supplementary sources and expert consultations refined data. Parameters were evaluated on Saaty's scale; Goepel's [88] framework assigned relative weights. This web-based AHP tool calculated the eigenvector, consistency ratio, and normalized weight via pairwise comparisons. Consistency was checked using Saaty's [89] criteria (< 0.10). This meticulous process assures robust, coherent decision-making with assigned weights. The consistency index and consistency ratio are computed by using Equations (7 and 8) since, according to Saaty's pairwise comparisons are consistent with the value < 0.10 [87]. This consistency check is essential to verify the reliability of the assigned weights. The results were obtained from the product of the vector sum and the assigned weightage.

$$CI = \frac{\lambda_{max} - n}{n-1} \tag{7}$$

$$CR = \frac{CI}{RI} \tag{8}$$

CI is the consistency index, λ_{max} is an eigenvalue, n is the number of influencing criteria, CR is the consistency ratio, and RI is the random index with a value of 7%.

In Fuzzy Logic, the evidential layers (thematic maps that control gold distribution) are assigned weights based on their impact on the mineralization process. Positive and negative weights are attributed to each class in a dataset, representing fuzzy membership values. These values range from 0 to 1, where 0 signifies full non-membership and 1 indicates full membership. Fuzzy membership values are established through a fuzzification process [90-91]. An additional fuzzy membership value can be assigned to a ''missing data'' class, representing areas with incomplete data coverage. This is useful when the dataset lacks comprehensive information.

Fuzzy MS Large and Fuzzy MS Small were used in the modeling process. These are membership functions used to evaluate the degree of an input's belongingness to "large" and "small," respectively. Fuzzy MS Large assigns higher membership values to inputs closer to being "large," making it suitable for modeling variables or objects associated with largeness, like size or quantity. In contrast, "Fuzzy MS Small" assigns higher membership values to inputs closer to being "small," making it useful for modeling variables or objects characterized by smallness.

After fuzzy membership values are assigned for each class in each dataset, the datasets are combined using the fuzzy sum operator to produce a mineral potential map [92]. The fuzzy sum incorporates contributions from the fuzzy membership values of each map. The combined fuzzy membership function is defined as the fuzzy membership value assigned to the ith map, with n maps to be amalgamated [92]. This function is ''increasive'', consistently yielding results equal to or greater than the largest input fuzzy membership value (Equation 9).

$$\mu_{comb}(x) = 1 - \prod_{i=1}^{n} 1 - \mu_i \tag{9}$$

5. Results

5.1 Principal component analysis (Crosta Technique)

The results of Principal Component Analysis (PCA) applied to a 5-band OLI image (bands 2, 4, 5, 6, and 7) are summarized in Table 2. The presence of iron oxide is indicated by a distinctive change in the PC5 image, with black pixels suggesting its potential existence. This pattern is attributed to OLI band 4's high negative eigenvalue (-0.560006) and OLI band 2's strong positive eigenvalue (0.798725), robustly signifying iron oxide. A 4-band composite image (bands 2, 4, 5, and 6) was also subjected to PCA Table 3. The resulting PC4 image reveals the presence of ferrous materials (bright pixels) due to OLI band 4's considerable negative eigenvalue (-0.535928) and OLI band 2's high positive eigenvalue (0.819305). This is also tagged the "F" image (Figure 4a).

Table 2: Eigen value results from 5-band composite PCA

	Band 2	Band 4	Band 5	Band 6	Band 7	Eigenvalues
PC1	-0.028986	-0.071419	-0.131102	-0.988368	-0.000515	92.57%
PC2	0.223838	0.529792	0.482199	-0.109147	0.651757	6.59%
PC3	-0.067554	-0.309299	-0.594682	0.102831	0.731813	0.73%
PC4	0.553652	0.552221	-0.590461	0.022284	-0.198446	0.09%
PC5	0.798725	-0.560006	0.219101	-0.01203	0.016782	0.03%

Table 3: Eigenvector loadings for the 2, 4, 5, and 6 band composite

	Band 2	Band 4	Band 5	Band 6	Eigenvalues
PC1	0.028981	0.071407	0.131091	0.988371	95.62%
PC2	-0.28318	-0.684996	-0.655472	0.14473	4.22%
PC3	-0.497703	-0.488328	0.715403	-0.045013	0.14%
PC4	0.819305	-0.535928	0.203395	-0.012282	0.03%

Furthermore, PCA was applied to a composite image of OLI bands 2, 5, 6, and 7, yielding the PC3 layer. This layer effectively captures hydroxyl alteration minerals as bright pixels, resulting from strong reflectance in OLI band 5 and absorption in OLI band 2 Table 4. This was classified as the "H" image (Figure 4b). To produce the Crosta image, "H" and "F" were combined to produce the "H+F" image (Figure 4c).

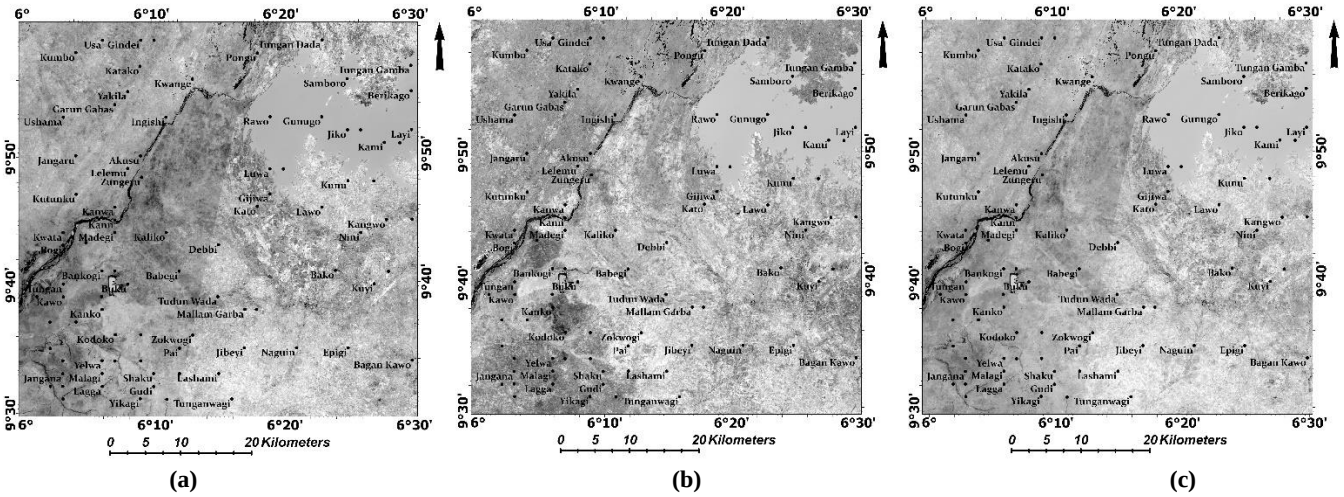

Figure 4: a: Principal component image resulting from selective PCA (Iron oxide (F) image), b: Principal component image resulting from selective PCA Hydroxyl ((H) image), c: Combination of H+F image, highlighting anomalous concentrations

Table 4: Eigenvector loadings for the 2, 5, 6, and 7 band composite.

Eigenvectors	Band 2	Band 5	Band 6	Band 7	Eigenvalues
PC1	-0.028395	-0.129967	-0.991111	0.001211	94.40%
PC2	0.258723	0.553569	-0.079041	0.78764	4.89%
PC3	-0.117436	-0.783897	0.106893	0.60024	0.65%
PC4	0.958366	-0.249351	0.005071	-0.139045	0.06%

Structural anomalies show changes in hydroxyl minerals due to the development of additional clay minerals in weak regions. An RGB composite using Crosta hydrothermal alteration was employed to comprehensively depict hydrothermal alterations (Figure 5). The RGB representation highlights argillitic and iron-oxide alteration zones in white to pale blue, indicating higher favourability for gold mineralization. Areas with more iron oxide than argillitic alteration are depicted differently. Deep blue pixels suggest intensely silicified rocks, corroborated by reflectance differences in bands 7 and 6 [93].

Hydroxyl alteration identification is facilitated by hydroxyl images, where dark pixels beside bright ones denote hydroxyl-altered regions. It's crucial to note that not all color hues correspond exclusively to hydrothermally altered rocks, as spectral responses from burned vegetation and SWIR bands also contribute. Consequently, identifying alterations around these dark areas is paramount, as it ensures accurate interpretation and differentiation between geologically altered formations and other influencing factors.

5.2 Surface lineaments

The results obtained from the hill shade process exhibited pronounced linear features, such as valley lineaments or ridges, which appeared more prominent than the surrounding terrain in the satellite images. This prominence was attributed to the interplay of dark-bright or shadow effects, where variations in input variable values led to differences in shadow formation, influencing the lineament patterns and, subsequently, identifying these linear features. All the imageries were overlaid to integrate the hill shade results and obtain a comprehensive representation of the earth's surface relief, creating a 3-dimensional view derived from four different angles.

5.3 Aeromagnetic data

The residual anomaly map depicting the area is presented in Figure 6a. Rocks displaying high magnetic properties are represented by purple and orange colors on the map, denoting significantly elevated values (measured in nanoTeslas, nT). Conversely, rocks with low magnetic values are depicted in blue and green. The gradual color transition on the map reflects the gradual variation in the magnetic field intensity over time. This map reveals the intricate superposition of perturbations within the earth with varying orders of magnitude. Magnetic signatures exhibit susceptibility values spanning from -27 nT to 70 nT. An interesting property of magnetic signatures is that the heterogeneous characteristics of the Earth's crust give rise to discernible "regional trends," displaying smooth continuity over extensive distances. Conversely, smaller-scale local

distortions, designated as anomalies, hold primary significance, yet local fields can mask them. Hence, these regional trends were removed from the data, focusing on the residuals holding fundamental exploration vectors.

The analysis of persistent short-wavelength anomalies in the map offers compelling insights into the potential presence of mineralized deposits characterized by distinctive structural attributes. Thorough scrutiny has been devoted to elucidating the diverse factors influencing the observed magnetic fabrics, encompassing changes in surface rock magnetic properties, generation of geological units at deeper depths, and the entombment of rock formations with stable magnetic susceptibilities. Moreover, discernible changes in hue serve as informative signs of sudden shifts in magnetic susceptibility, a common occurrence in faults, volcanic dikes, and mineralized zones.

The extraction of lineaments was based on the digitization of magnetic minima and maxima using the THG (Figure 6b), Tilt (Figure 6c), and FVD Figure 6d derivative maps. The derivative maps prominently revealed linear or curvilinear features, accentuated by fragmented aeromagnetic highs or lows, indicative of profound structural anomalies.

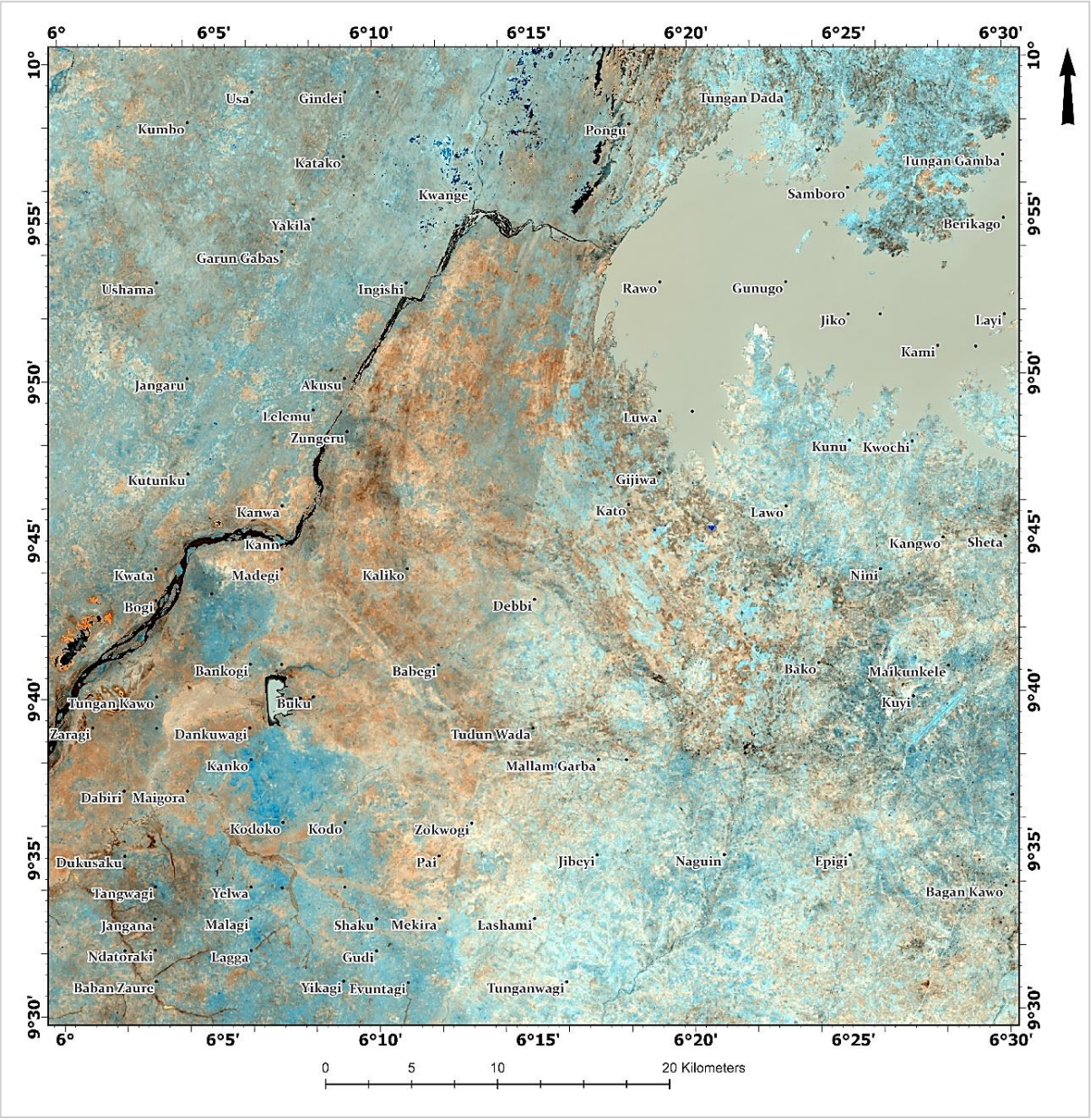

Figure 5: RGB combination using H, H+F, and F images, the Crosta composite image

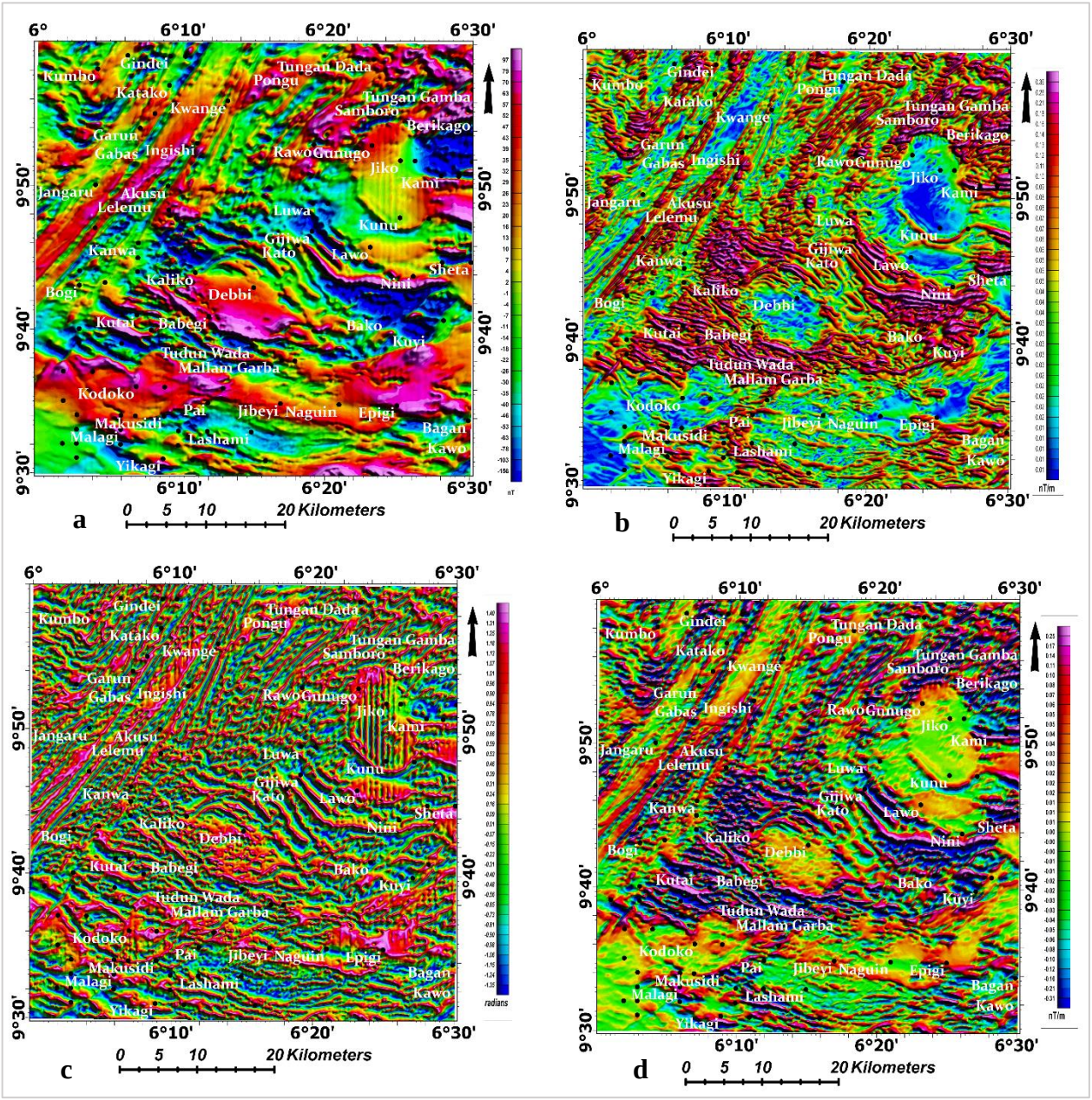

Figure 6: a: Residual magnetic intensity (Reduced to the Equator) map, b: Total Horizontal Gradient (THG) derivative map, c: Tilt angle (TDR) derivative map, d: First Vertical Derivative (FVD) map

A composite of remote sensing lineaments and magnetic lineaments has been processed to produce a lineament density map of the study area (Figure 7). Utilizing information drawn from the lineament density (Figure 6), an analysis of geological structure zonation was conducted, characterized by sets of lineaments. Zones with potential mineralization were found at the intersection of two density zones, indicating areas of weaker zones resulting from tectonic processes that gave rise to geological structures in that region. These weak zones facilitated the occurrence of hydrothermal processes, leading to the formation of valuable minerals. Hydrothermal systems were identified as zones of hot fluid circulation (ranging from 50 °C to 500 °C), occurring laterally and vertically at various temperatures and pressures beneath the earth's surface. The lithostructural concept was applied to establish a connection between the lineament density information and areas with mineral potential. This concept encompassed three fundamental components, namely lithology control, hydrothermal breccias control, and fault control, as proposed by Sillitoe [94].

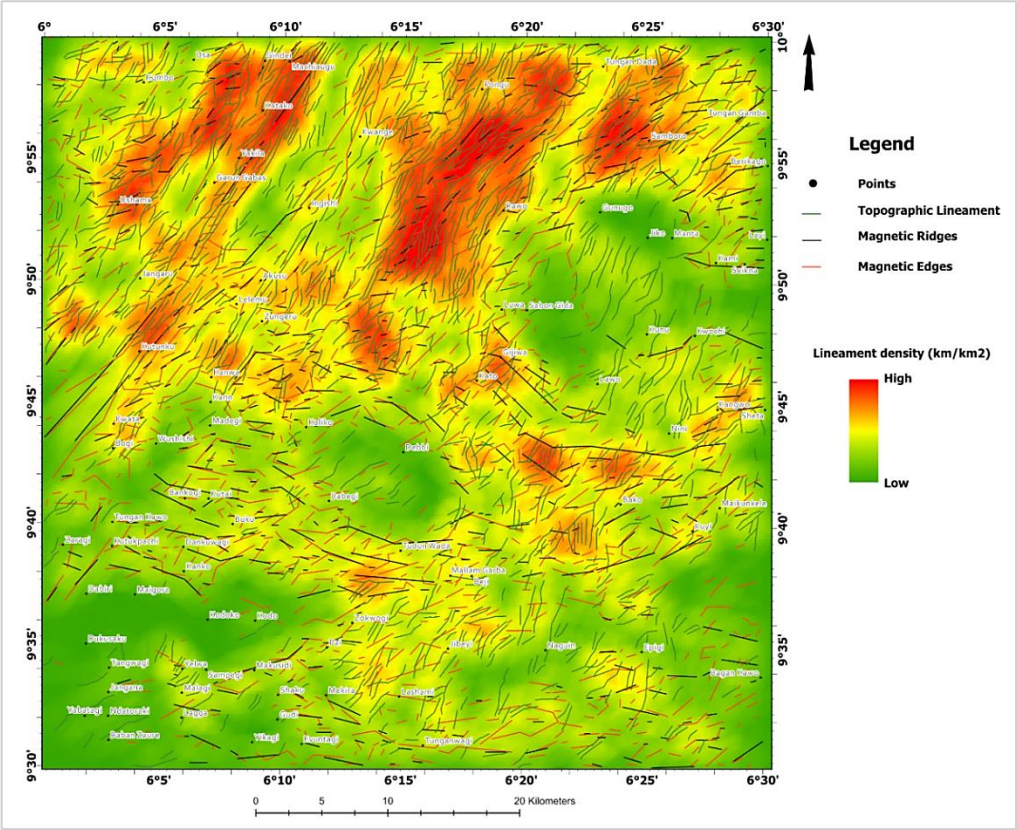

Figure 7: Composite lineament density map

5.4 Gamma-ray spectrometry (radiometric data)

5.4.1 Potassium map (%K)

The potassium (%K) map (Figure 8a) provides information on potassium concentrations ranging from 0.03% to 5.41% Figure 8a. These variations correspond to different lithological units and regional characteristics. It is important to note that the content of radioelements can be influenced by various factors, such as alteration, weathering, environmental conditions, and hydrothermal processes. Signature modifications often lead to increased potassium values, while degradation typically diminishes the strength of these alterations [95].

The radiometric map reveals multiple potassium anomalies. The magenta color-coded contours indicate extremely high potassium values, while the blue color-coded contours represent low potassium values. Orange to yellow shades are associated with relatively low potassium values, whereas red indicates moderately high to high potassium values. In the research region's eastern quadrant, we observe extremely high and moderately high potassium values. In contrast, the northwest quadrant of the study area exhibits lower potassium values. These variations are closely related to the identified schistose lithology in the region, associated with lower potassium values.

5.4.2 Thorium (eTh) map

Thorium, being relatively immobile during mineralization processes and experiencing only partial depletion in regions of intense K-alteration and silicification, is typically unaffected by modifications to the system. The concentration map displays eTh (equivalent thorium) values ranging from 4.26 ppm to 31.56 ppm (Figure 8b). To this analysis, eTh values in the research region are broadly classified as high (>18 ppm), relatively high (14–18 ppm), relatively low (10–14 ppm), and low (<10 ppm).

The map's red to magenta color codes indicate areas with high eTh concentrations evenly distributed across the research region. These high concentrations can be attributed to granitic rocks and migmatite gneiss lithology. On the other hand, lower eTh concentrations are associated with the schistose rock lithology in the study area.

5.4.3 Uranium (eU) map

Figure 6c illustrates the map displaying the concentration of eU (equivalent uranium). Uranium holds significant importance in hydrothermal and other geological activities. It is important to remember that potassium enrichment may or may not occur simultaneously with uranium enrichment. The map displays eU concentrations ranging from 0.44 ppm to 7.44 ppm, revealing several anomalous signals (Figure 8c). An analysis of the equivalent eU concentration map suggests the presence of a linear (sheet-like) concentration trend. The alignment of structures in the studied region appears to be relatively parallel to these concentration patterns. Furthermore, the high eU concentrations can be attributed to Pan African older granites and the meta-sedimentary/meta-volcanic lithologies in the region, specifically the migmatite gneiss.

5.4.4 Radiometric ratio map

Regions exhibiting hydrothermal alteration are identifiable by red to magenta colors, indicating high values of over 0.3, as depicted in the K/eTh ratio map (Figure 8d). These areas within the study area have been delineated as alteration zones. This pattern is observed across the research area, particularly in regions with various rock types. Consequently, zones exhibiting high values in the K/eTh ratio serve as reliable indicators of hydrothermal alteration.

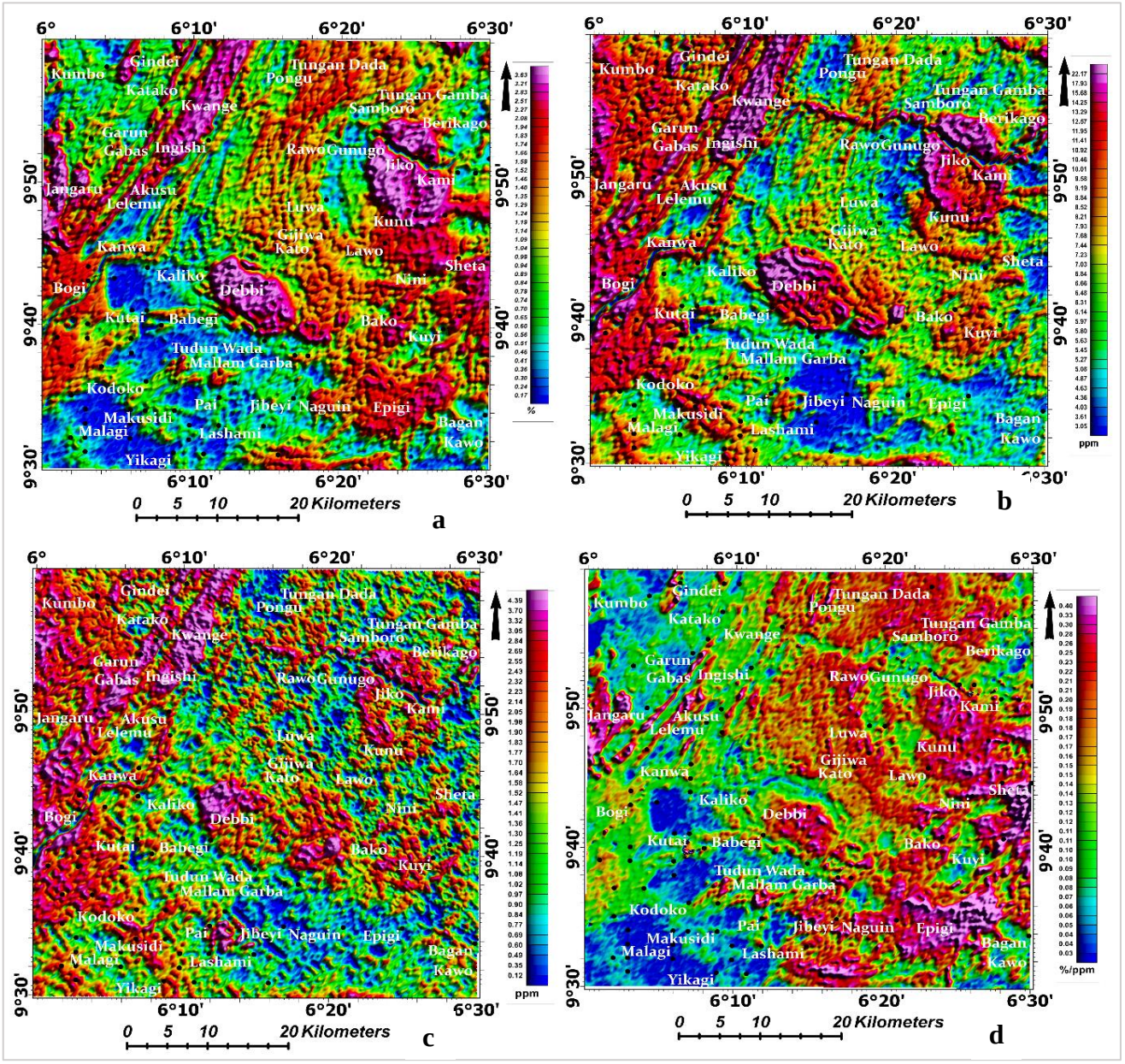

Figure 8: a: Potassium concentration map (%K), b: Equivalent Thorium concentration (eTh) map, c: Equivalent Uranium concentration (eU) map**,** d: Potassium / equivalent thorium concentration ratio map

5.4.5 Ternary maps

The RGB ternary map (Figure 9a) is an effective tool for identifying anomalies. Bright blue spots on the map indicate places where the uranium count rate is noticeably greater than the count rates of the other two elements. Bright green areas depict locations with different proportions of Th, U, and K, whereas bright red spots denote zones with increased potassium count rates. This color-coded format makes it easy to recognize and classify distinct anomalies. Black to brown zones are associated with earlier granites and sediments, indicating lower K, Th, and U. Red zones correspond to increased K concentrations, green zones indicate higher Th content and blue zones reflect higher U concentrations. Cyan zones exhibit low potassium levels and elevated levels of uranium and thorium. Magenta components, characterized by low thorium, display high Potassium and uranium content. Yellow areas denote high uranium levels and low thorium levels. A few white zones with high K, Th, and U values have been linked to exposed granitic bedrock.

A ternary map (Figure 9b) was utilized, incorporating Potassium (red), thorium (green), and TDR components. Using this map, we could spot several patterns: radioelement and TDR depletion were seen in granitic rock units, which is probably

related to intrusions rich in quartz. High TDR values were seen near the margins of granitic intrusions, shear zones, and the identified magnetic lineaments. Still, high eTh (equivalent thorium) and TDR values were seen in the interior of granitic intrusions. These findings align with the descriptions of hydrothermal processes and the presence of K-feldspar provided by Biondi et al. [96] and Hueck et al. [97]. The ternary map also showed that rare metal mineralization frequently occurred in zones with high eTh and K, which correlated to regions with high K and TDR values or zones with high K, eTh, and TDR values. This shows that structural and hydrothermal processes played a role in developing these mineralized zones.

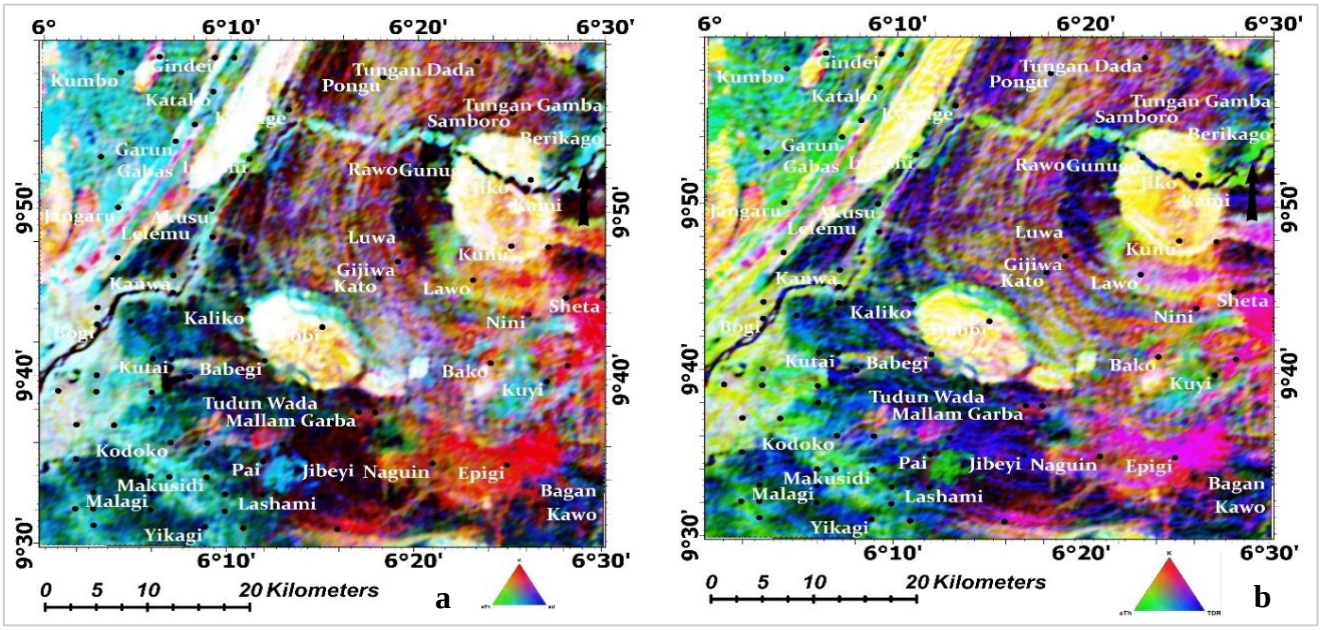

Figure 9: a: RGB ternary map of Potassium, equivalent thorium, and equivalent uranium concentrations, b: RGB ternary map incorporating Potassium (red), thorium (green), and TDR components

5.5 GIS modelling

The successful implementation of MCDA using ArcGIS Pro has yielded valuable insights into delineating mineral potential zones. The systematic approach has generated a comprehensive suitability map that effectively captures the varying degrees of mineral prospectivity across the study area. Field verification of the suitability map has been an integral part of our methodology, and it plays a crucial role in ensuring the accuracy and usability of the results. Through rigorous field checks and corrections, inconsistencies were addressed, ensuring higher accuracy of the final suitability map. Five distinct mineral-prospective zones: "Very Good," "Good," "Moderate," "Poor," and "Very Poor" have been delineated. These zones provide a spatial representation of the varying levels of mineral potential across the study area.

6. Discussion

In geological exploration, target generation is an important stage involving high risk, and defining prospective areas requires geological information, which is sometimes unavailable or inaccurate. Furthermore, field reconnaissance is time-consuming and can be difficult and expensive. Remote sensing has been successfully applied to map hydrothermal alteration zones associated with mineralization in different parts of the world [2, 98, 99]. Remote sensing data and other gathered geological data, such as geochemical and geophysical information, can be integrated to produce a potential mineral occurrence map [29,100].

In this investigation, feature-oriented principal component analysis (FPCA) was applied to Landsat 8 data to map hydroxyl-bearing and iron oxide minerals and extract structural lineaments, defining prospective targets in the study area. Hydrothermal alteration minerals were mapped using PCA algorithms applied to the spectral bands of Landsat 8 based on the spectral absorption characteristics for iron oxides and hydroxyl-bearing minerals by implementing RGB combinations. RGB combinations of different FPCA-derived products could distinguish different features and enhance the alteration of rock outcrops. However, this imagery analysis method strongly influences noise, and it is difficult to separate signals from different mineral compositions, making this type of analysis the most challenging to interpret. For this method, the best results can be obtained in remote areas without signal noise from urban areas and less vegetated regions. Prior to processing these, vegetation suppression was applied to the imagery to enhance results [101].

Selective PCA outputs proved the most effective and reliable in identifying iron oxides and hydroxyl-bearing minerals. It demonstrated the capability to discriminate different features efficiently and highlight potentially hydrothermally altered areas by separating hydroxyl-bearing minerals and iron oxides. The combination of selective PCA outputs in an RGB image produced a better-quality image, enhancing the identification of alteration types and intensities Figure 3. The distinctive changes observed in the PC5, PC4, and PC3 images provided valuable insights into the spatial distribution of these alterations. The presence of bright pixels and specific absorption features in different bands indicated the potential existence of these

alterations in the study area [101]. Identifying these hydrothermal alteration zones offers significant implications for potential mineralization, as they often indicate subsurface fluid activity and the formation of ore deposits.

Lineaments were extracted using a semi-automatic interpretation of remote sensing imagery, SRTM elevation model, and aeromagnetic data. Geological lineaments such as faults and joints are interesting because they can serve as conduits for mineralizing fluids. Textural characteristics of structural features are recognizable by multispectral imagery analysis, allowing the identification of lineaments. Subsurface structural features are mostly delineated by the aeromagnetic lineaments. It is important to mention that some mapped features may not be geologic. Still, a good correlation is verified between the published geological maps Figure 2 and the interpreted lineaments (Figure 7).

The surface lineaments observed in the mapping mainly consist of peaks, valleys, and drainage channels. Adjustments were made to the sun illumination angles to enhance their visibility in the SRTM DEM, resulting in diverse lineaments derived from different perspectives of the same region, especially those perpendicular to the lighting angle. This diversity can be attributed to the association between digitized lineaments and fracture zones, drainage channels, and geomorphological features. Combining all the surface lineaments obtained during the study generated a composite remote-sensing lineament.

Various magnetic lineaments with distinct orientations were identified in the area and categorized based on their orientations. The dominating trend was the ENE-SSW direction, alongside a secondary trend in the NW-SE direction. A major regional fault with a NE-SW trend was identified in the northwest of the research area, intersecting some lineaments and lithological boundaries. According to the aeromagnetic maps, these structures serve as significant conduits for mineralization fluids.

The ENE-SSW trends in the study area are attributed to the Central African Shear Zone (CASZ), formed during the Pan-African orogenic cycle due to tectonic events [102,103]. These trends align with broader mylonite belts developed during the formation of the South Atlantic Ocean in the Cretaceous epoch. Additionally, the ENE-SSW trend functions as a dextral shear zone, as suggested by Jorgensen and Bosworth [104]. The NE-SW lineaments, on the other hand, are minor trends likely induced by the African plate sliding over a mantle plume or shearing motions along pre-existing ENE-WSW faults in the Pan-African basement. Figure 5 presents a lineament density map for the research region, combining magnetic and remote sensing lineaments.

The analysis reveals a significant correlation between hydrothermal alterations and lineaments in the study area. The lineament density map, derived from a combination of magnetic and remote sensing lineaments, exhibits spatial patterns corresponding to areas of pronounced hydrothermal activity. Regions with elevated lineament density tend to coincide with heightened hydrothermal alterations, indicating that lineaments could be influenced by subsurface geological processes associated with hydrothermal activity. Conversely, regions with lower lineament density align with areas of reduced or negligible hydrothermal alterations. These findings underscore the relevance of lineament analysis in identifying potential hydrothermal zones and understanding the geological processes governing their formation. The observed correlation between hydrothermal alterations and lineaments provides valuable insights for future research and exploration efforts, contributing to a more comprehensive understanding of the geological context and implications for gold mineral resource assessments.

Gamma-ray spectrometry data analysis allowed for mapping Potassium, thorium, and uranium concentrations in the study area. The potassium map demonstrated a wide range of concentrations, with elevated values occurring in areas associated with hydrothermal alteration zones. The high concentrations of Potassium often indicate the presence of clay minerals, commonly formed during hydrothermal alteration processes. The thorium map revealed varying concentrations across the study area, with high values concentrated in regions dominated by granitic rocks and migmatite gneiss. The presence of thorium is often associated with felsic igneous rocks and metamorphic processes. Uranium concentrations were also notable in specific areas, with higher values corresponding to regions with diverse lithologies and structural complexities. The correlation between elevated Potassium and uranium concentrations further supports the presence of potential mineralization.

Integrating multiple datasets into a GIS framework allowed for systematically evaluating mineral prospectivity in the study area. Multi-Criteria Decision Analysis (MCDA) based Analytic Hierarchy Process (AHP) and Fuzzy Logic were used to generate mineral potential zones maps for mineralization in the study area. Incorporating various criteria, including lithological characteristics, lineament density, and radioelement concentrations, enabled a comprehensive assessment of potential mineralization zones Table 5. The observed correlation between hydrothermal alterations, lineaments, and elevated mineral concentrations suggests that structural controls play a critical role in the formation and localization of mineralization zones. The presence of lineaments intersecting hydrothermal alteration zones underscores the role of these structural features as pathways for mineralizing fluids. Additionally, the relationship between lithological boundaries, major faults, and hydrothermal activity indicates favorable conditions for the concentration of ore-forming elements.

Table 5: Pairwise comparisons used to calculate thematic priorities using the Analytic Hierarchy Process

Priorities			**Decision Matrix**				
Thematic map	Priority	Rank	1	2	3	4	5
Hydrothermal alteration	32	1	1	2	4	5	5
Radiometric alteration	28	2	0.5	1	8	6	4
Lineament Density	18	3	0.25	0.12	1	2	3
Lithology	8	4	0.2	0.17	0.5	1	2
Source Parameter Imaging	5	5	0.2	0.25	0.33	0.5	1
Number of comparisons = 10		Consistency ratio CR = 9.1%		Principal eigen value = 5.411			

As a product of the AHP, the resulting potential zones map delineated five distinct mineral-prospective zones, each with varying levels of mineralization potential (Figure 10a). Notably, the "Very Good" to "Good" zones predominantly align with the NNE direction, with some extent of occurrence in the NW quadrant of the study area. This spatial correlation with lithological characteristics and lineament features suggests a strong influence of these factors on mineral prospectivity. Likewise, the Fuzzy Overlay prospective zone map (Figure 10b) has been classified into five using the same rating as the AHP model. Examining the spatial correlation between established gold mining sites and each predictive model indicates a notable connection with regions exhibiting high favourability. Within these models, approximately 76% of total gold mineralization appears to be within the most favorably projected zones. The statistical validation employing the ROC/AUC metric, as depicted in Figure 11, indicates considerable reliability for both models, with predictive accuracies surpassing 70%. A comparative evaluation of predictive precision between both models highlights the Fuzzy Logic model as showcasing the highest predictive efficacy, as evidenced by a prediction level of 78.3%. Table 6 shows the validation results of gold mining sites from the models.

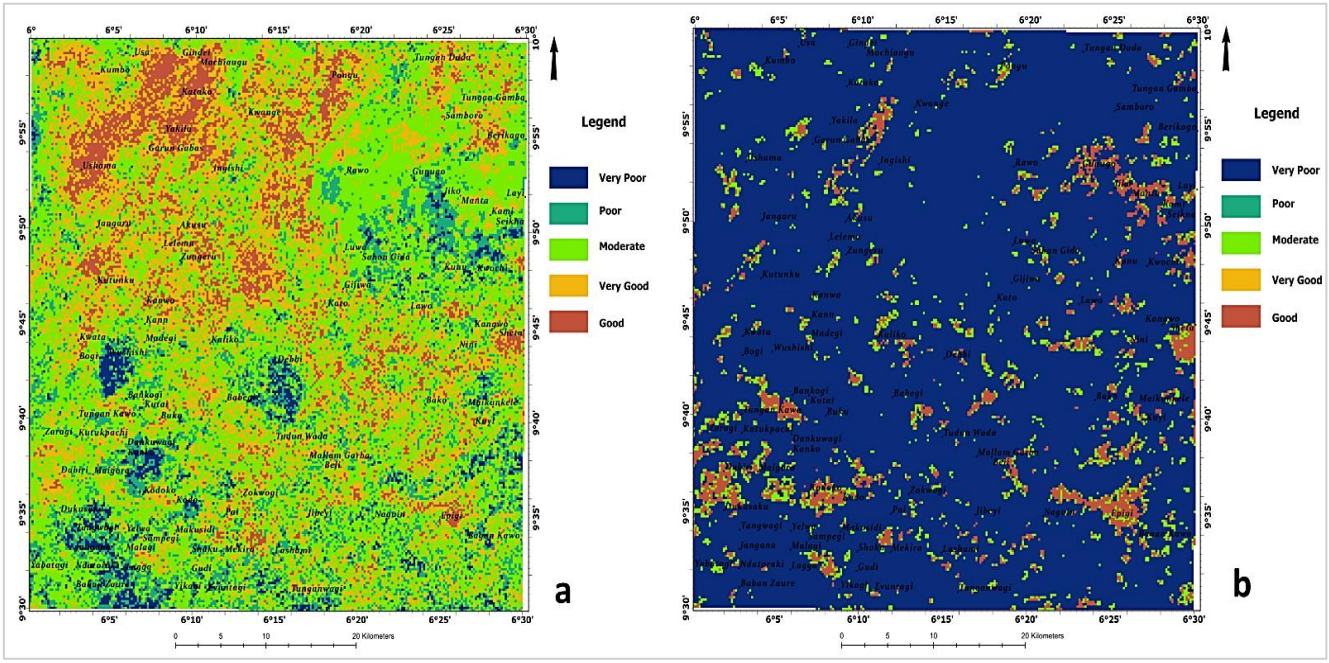

Figure 10: a: Mineralization potential zones map from the AHP model, b: Mineralization potential zones map from Fuzzy Overlay model

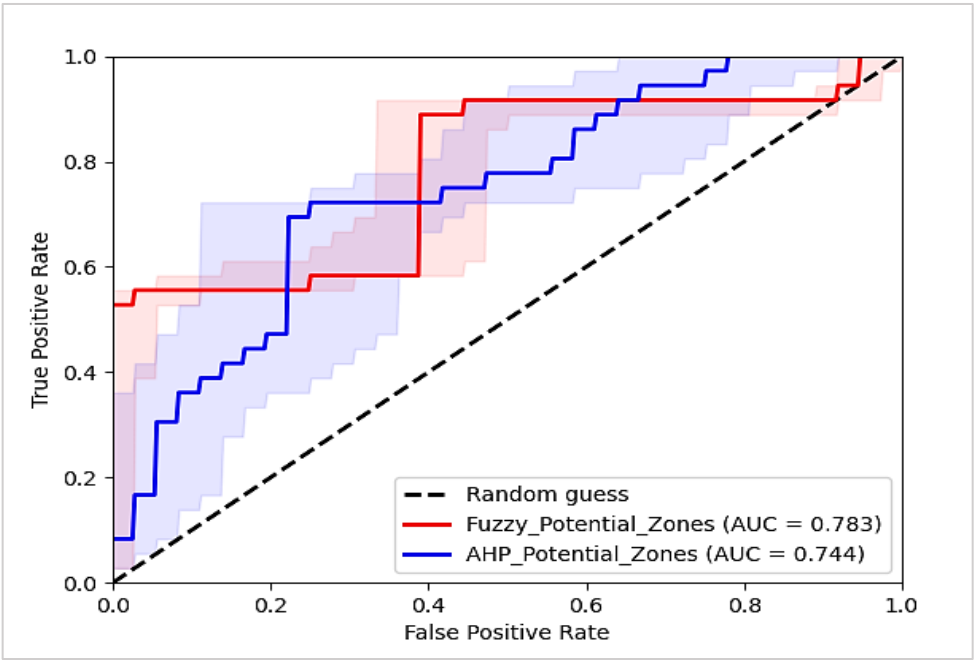

Figure 11: Validation and accuracy assessment of mineralization potential zones map ROC/AUC metrics

Table 6: Validation results from existing gold mines

ID	Easting	Northing	Very poor	Poor	Moderate	Good	Very Good	Validation
	200422.7	1074807					✓	Pass
2	207996.3	1070174				✓		Pass
3	205851.5	1069373			✓			Pass
4	208554.2	1070124					✓	Fail
5	184072.2	1103386		✓				Pass
6	176613.2	1091098			✓			Pass
7	178841.8	1096229					✓	Fail
8	176927.4	1093540	✓					Pass
9	177108	1091530				✓		Pass
10	176874.8	1091019	✓					Pass
11	177091.3	1091020				✓		Pass
12	186140.1	1084293		✓				Pass
13	186735.8	1093108				✓		Pass
14	214251.9	1052011				✓		Pass
15	191195.3	1097316					✓	Fail
16	194815.4	1076823	✓					Pass
17	175550.8	1102616				✓		Fail
18	219559.6	1060902				✓		Pass
19	198247.2	1062294		✓				Pass
20	176209.2	1083439					✓	Fail
21	199760	1054781				✓		Fail
22	182602.6	1096956		✓				Pass
23	213571.6	1076900				✓		Pass
24	218042.9	1058892			✓			Pass
25	181166.6	1070533	✓					Fail
26	224373.6	1054104				✓		Fail
27	220324.1	1097324				✓		Pass
28	212353.8	1084507			✓			Pass
29	205793.8	1102581			✓			Pass
30	206958.7	1055127					✓	Pass
31	213739.3	1094760				✓		Fail
32	200904.2	1087767	✓					Pass
33	186665.4	1091373				✓		Pass
34	219198.8	1080126				✓		Pass
35	192203.3	1081180		✓				Pass
36	186339.5	1061835					✓	Pass
						% Agreement = 27/36 = 75%		

7. Conclusion

This study presents a novel approach for mineral exploration in Zungeru, North-Central, Nigeria, by integrating remote sensing, geophysical data, and GIS modeling. This cost-effective and efficient methodology allows for identifying potential hydrothermal alteration zones, mineral-prospective areas, and mineralization pathways that were not previously documented in detail. This represents a significant advancement compared to traditional exploration methods in the region. The resulting suitability map provides a valuable spatial exploration tool for directing future efforts toward zones with the highest mineralization probability. This targeted approach maximizes the chances of successful discovery while minimizing exploration costs and environmental impact. Our findings contribute substantially to a more comprehensive understanding of the geological framework and mineralization potential in Zungeru, North-Central Nigeria. This knowledge base will be crucial for the region's sustainable mineral exploration and resource development. While the study acknowledges limitations associated with remote sensing and data subjectivity, it lays a strong foundation for further exploration. Future research can validate these findings through more detailed field verification and sampling while refining the GIS criteria and incorporating additional datasets for enhanced accuracy and reliability in mineral prospectivity assessments.

Author contributions

Conceptualization, Abdullahi, S. and Ejepu, J.S.; data curation, Ejepu, J.S..; formal analysis, Ejepu, J.S.; investigation, Abdullahi, S.; methodology, Abdullahi, S. and Ejepu, J.S.; project administration, Ejepu, J.S., resources, Abdullahi, S.; software, Ejepu, J.S.; supervision, Ejepu, J.S.; validation, Abdullahi, S. and Ejepu, J.S.; visualization, Ejepu, J.S.; writing—original draft preparation, Ejepu, J.S.; writing—review and editing, Abdullahi, S. and Ejepu, J.S. All authors have read and agreed to the published version of the manuscript.

Funding

This research received no specific grant from any public, commercial, or other sector funding agency.

Data availability statement

The data supporting this research's findings are available on request from the corresponding author.

Conflicts of interest

The authors have no financial interests, directly or indirectly, regarding the work being submitted for publication.

References

[1] L. Adebiyi, A. Eluwole, F. Akindeji, N. Salawu, Integrated geophysical methods for delineating crustal structures and hydrothermal alteration zones for mineral exploration projects in parts of west-central, Nigeria, Model. Earth Syst., Environ., 8 (2021) 2977–2989. http://dx.doi.org/10.1007/s40808-021-01275-5

[2] F. Sabins, Remote Sensing for Mineral Exploration, Ore Geol. Rev., 14 (1999) 157-183. http://dx.doi.org/10.1016/S0169-1368(99)00007-4

[3] C. Okeke, V. Ukaegbu, N. Egesi , Remote sensing signature of geological structures inferred on Landsat imagery of Afikpo area Southeastern Nigeria, J. Geol. Min. Res., 11 (2019) 1-13. http://dx.doi.org/10.5897/JGMR2018.0305

[4] A. Oyawale, F. Adeoti, T. Ajayi, A. Omitogun, Applications of remote sensing and geographic information system (GIS) in regional lineament mapping and structural analysis in Ikare Area, Southwestern Nigeria, J. Geol. Min. Res., 12 (2020) 13-24. http://dx.doi.org/10.5897/JGMR2019.0310

[5] A. Pour, B. Zoheir, B. Pradhan, M. Hashim, Editorial for the special issue: multispectral and hyperspectral remote sensing data for mineral exploration and environmental monitoring of mined areas, Remote, Sens., 13 (2021) 519. https://doi.org/10.3390/rs13030519

[6] C. Okpoli, J. Ogbole, O. Victor, G. Okanlawon, Mineral exploration of Iwo-Apomu Southwestern Nigeria using aeromagnetic and remote sensing, Egypt. J. Remote. Sens. Space .Sci. , 25 (2022) 371-385. https://doi.org/10.1016/j.ejrs.2022.03.004

[7] F. Ruitenbeek, T. Cudahy, F. Meer, M. Hale, Characterization of the hydrothermal systems associated with Archean VMS-mineralization at Panorama, Western Australia, using hyperspectral, geochemical and geothermometric data, Ore Geol. Rev., 45 (2012) 33-46. https://doi.org/10.1016/j.oregeorev.2011.07.001

[8] J. Uwiduhaye, J. Ngaruye, H. Saibi, Defining potential mineral exploration targets from the interpretation of aeromagnetic data in western Rwanda, Ore Geol. Rev., 128 (2021) 103927. https://doi.org/10.1016/j.oregeorev.2020.103927

[9] R. Frutuoso, A. Lima, A. Teodoro, Application of remote sensing data in gold exploration: Targeting hydrothermal alteration using Landsat 8 imagery in northern Portugal, Arab. J. Geosci., 14 (2021) 1-18. https://doi.org/10.1007/s12517-021-06786-0

[10] M. Fustic, R. Nair, A. Wetzel, R. Siddiqui, W. Matthews, et al., Bioturbation, heavy mineral concentration, and high gamma-ray activity in the Lower Cretaceous McMurray Formation, Canada, Palaeogeogr. Palaeoclimatol. Palaeoecol., 564 (2021) 110187. https://doi.org/10.1016/j.palaeo.2020.110187

[11] L. Rowan, A. Goetz, R. Ashley, Discrimination of hydrothermally altered and unaltered rocks in visible and near infrared multispectral images, Geophysics, 42 (1977) 522-535. https://doi.org/10.1190/1.1440723

[12] A. Pour, M. Hashim, Hydrothermal alteration mapping from Landsat-8 data, Sar Cheshmeh copper mining district, south-eastern Islamic Republic of Iran, J. Taibah Univ. Sci., 9 (2015) 155-166. https://doi.org/10.1016/j.jtusci.2014.11.008

[13] M. Fuertes-Fuente, A. Cepedal, A. Lima, A. Doria, M. dos Anjos Ribeiro, A. Guedes, The Au-bearing vein system of the Limarinho deposit (northern Portugal): Genetic constraints from Bi-chalcogenides and Bi–Pb–Ag sulfosalts, fluid inclusions and stable isotopes, Ore Geol. Rev., 72 (2016) 213-231. https://doi.org/10.1016/j.oregeorev.2015.07.009

[14] K. Nikolakopoulos, P. Lampropoulou, D. Papoulis, A. Rogkala, P. Giannakopoulou, P. Petrounias, Combined use of remote sensing data, mineralogical analyses, microstructure studies and geographic information system for geological mapping of Antiparos Island (Greece), Geosciences, 8 (2018) 96. https://doi.org/10.3390/geosciences8030096

[15] J. Cardoso-Fernandes, A. Teodoro, A. Lima, M. Perrotta, E. Roda-Robles, Detecting Lithium (Li) mineralization from space: Current research and future perspectives, Appl. Sci., 10 (2020) 1785. https://doi.org/10.3390/app10051785

[16] A. Funedda, S. Naitza, C. Buttau, F. Cocco, A. Dini, Structural controls of ore mineralization in a polydeformed basement: Field examples from the Variscan Baccu Locci shear zone (SE Sardinia, Italy), Minerals, 8 (2018) 456. https://doi.org/10.3390/min8100456

[17] J. Tuduri, A. Chauvet, L. Barbanson, M. Labriki, M. Dubois, P. Trapy, L. Maacha, et al., Structural control, magmatic-hydrothermal evolution, and formation of hornfels-hosted, intrusion-related gold deposits: Insight from the Thaghassa deposit in Eastern Anti-Atlas, Morocco, Ore Geol. Rev., 97 (2018) 171-198. https://doi.org/10.1016/j.oregeorev.2018.04.023

[18] A. Chauvet, Structural control of ore deposits: The role of pre-existing structures on the formation of mineralized vein systems, Minerals, 9 (2019) 56. https://doi.org/10.3390/min9010056

[19] F. Meer, et al., Multi- and hyperspectral geologic remote sensing: A review, Int. J. Appl. Earth Obs. Geoinf., 14 (2012) 112-128. https://doi.org/10.1016/j.jag.2011.08.002

[20] J. Wambo, et al., Identifying high potential zones of gold mineralization in a sub-tropical region using Landsat-8 and ASTER remote sensing data: a case study of the Ngoura-Colomines goldfield, eastern Cameroon, Ore Geol. Rev., 122 (2020) 103530. https://doi.org/10.1016/j.oregeorev.2020.103530

[21] A. Shebl, M. Abdellatif, S. Elkhateeb, Á. Csámer, Multisource data analysis for gold potentiality mapping of Atalla area and its environs, Central Eastern Desert, Egypt, Minerals, 11 (2021) 641. https://doi.org/10.3390/min11060641

[22] A. Pour, M. Hashim, Identification of hydrothermal alteration minerals for exploring of porphyry copper deposit using ASTER data, SE Iran, J. Asian Earth Sci., 42 (2011) 1309-1323. https://doi.org/10.1016/j.jseaes.2011.07.017

[23] A. Misi, et al, Review of the geological and geochronological framework of the Vazante sequence, Minas Gerais, Brazil: Implications to metallogenic and phosphogenic models, Ore Geol. Rev., 63 (2014) 76-90. https://doi.org/10.1016/j.oregeorev.2014.05.002

[24] M. Monsef, et al., Role of Magmatism and Related-Exsolved Fluids during Ta-Nb-Sn Concentration in the Central Eastern Desert of Egypt: Evidences from Mineral Chemistry and Fluid Inclusions, J. Earth Sci., 34 (2023) 674-689. https://doi.org/10.1007/s12583-022-1778-y

[25] G. Hunt, Spectral signatures of particulate minerals in the visible and near infrared, Geophysics, 42 (1977) 468- 671. https://doi.org/10.1190/1.1440721

[26] R. Girija, S. Mayappan, Mapping of mineral resources and lithological units: A review of remote sensing techniques, Int. J. Image Data Fusion., 10 (2019) 79-106. https://doi.org/10.1080/19479832.2019.1589585

[27] J. Hamisi, D. MacKenzie, et al., Hydrothermal footprint of the Birthday reef, Reefton goldfield, New Zealand , New Zealand J. Geol. Geophys., 60 (2017) 59-72. https://doi.org/10.1080/00288306.2016.1274332

[28] D. Groves, M. Santosh, R. Goldfarb, L. Zhang, Structural geometry of orogenic gold deposits: Implications for exploration of world-class and giant deposits, Geosci. Front., 9 (2018) 1163-1177. https://doi.org/10.1016/j.gsf.2018.01.006

[29] A. Pour, et al., Evaluation of ICA and CEM algorithms with Landsat-8/ASTER data for geological mapping in inaccessible regions, Geocarto Int., 34 (2019) 785-816 https://doi.org/10.1080/10106049.2018.1434684

[30] L. Liu, Y. Li, J. Zhou, et al., Gold-copper deposits in Wushitala, Southern Tianshan, Northwest China: Application of ASTER data for mineral exploration, Geol. J., 53 (2018) 362–371. https://doi.org/10.1002/gj.2989

[31] A. Abdelnasser, et al., REE geochemical char- acteristics and satellite-based mapping of hydrothermal alteration in Atud gold deposit, Egypt, J. African Earth Sci., 145 (2018) 317–330. https://doi.org/10.1016/j.jafrearsci.2018.01.013

[32] B. Fagbohun, et al., Identifying geochemical anomalies and spatial distribution of gold and associated elements in the Zuru Schist Belt, northwest Nigeria, Arab. J. Geosc., 14 (2021) 1-20. https://doi.org/10.1007/s12517-021-06828-7

[33] I. Garba, S. Akande, The origin and significance of non-aqueous CO2 fluid inclusions in the auriferous veins of Bin Yauri, northwestern Nigeria, Miner. Deposita, 27 (1992) 249-255. https://doi.org/10.1007/BF00202550

[34] A. Darma, et al., Appraisal of lead (Pb) contamination and potential exposure risk associated with agricultural soils and some cultivated plants in gold mines, Environ. Syst. Res., 11 (2022) 1-12. https://doi.org/10.1186/s40068-022-00259-3

[35] O. Ohioma, Detection of Sulphide Deposit Using Uranium/Potassium Ratio Map, Ghana J. Geogr., 12 (2020) 145-158. https://doi.org/10.4314/gjg.v12i1.8

[36] Burke, K. C & Dewey, J. F. Orogeny in Africa, In Dessauvagie, T. F. J. and Whiteman, A. J. (Eds.). African Geology (1972) 583-608

[37] N. Grant , Geochronology of Precambrian basement rocks of Ibadan, SouthWestern Nigeria, Earth Planet. Sci. Lett., 10 (1970) 29-38. https://doi.org/10.1016/0012-821X(70)90061-0

[38] J. Bertrand, R. Caby, Geodynamic evolution of the Pan-African orogenic belt: a new interpretation of the Hoggar Shield (Algerian Sahara), Geol. Rundsch, 67 (1978) 357-388. https://doi.org/10.1007/BF01802795

[39] M. Rahaman, Recent advances in the study of the Basement Complex of Nigeria. Precambrian Geology of Nigeria, Geol. Survey of Nigeria Publications, (1988) 11-43.

[40] M. Oyawoye, The Geology of the Nigerian Basement Complex, Nigeria, J. Mining Geol. Metal Soc., 1 (1972) 7-102.

[41] Mccurry, P. Geology of degree Sheet 21 (Zaria). Overseas Geology and Mineral Resources, 45 HMSO, London. (1973).

[42] M. Olade, A. Elueze, Petrochemistry of the Ilesha amphibolites and Precambrian crustal evolution in the Pan-African domain of SW Nigeria, Precambrian Res., 8 (1979) 303-318. https://doi.org/10.1016/0301-9268(79)90033-0

[43] N. Grant, Structural distinction between a metasedimentary cover and an underlying basement in the 600 Ma old in the Pan-African domain of north-western Nigeria, Bulletin, 89 (1978) 50–58. https://doi.org/10.1130/0016-7606(1978)89<50:SDBAMC>2.0.CO;2

[44] Holt, R. The Geotectonic Evolution of the Anka Belt in the Precambrian Basement Complex of N.W. Nigeria, Unpublished Ph. D. Thesis, The Open University. 1982. https://doi.org/10.21954/ou.ro.000100d8

[45] D. Turner, Upper Proterozoic schist belts in the Nigerian sector of the Pan-African province of West Africa, Precambrian Res. , 21(1983) 55-79. https://doi.org/10.1016/0301-9268(83)90005-0

[46] Ajibade, A. C., Anyanwu, N. P. C., Okoro, A. U., & Nwajide, C. S. The Geology of Minna Area (Explanation of 1: 250,000 Sheet 42, Minna). Bulletin, (43) (2008).

[47] A. Ajibade, M. Woakes, M. Rahaman, Proterozoic crustal development in the Pan-African regime of Nigeria, In Kroner, A. (Ed.), Precambrian Plate Tectonics, Elsevier, Amsterdam, 17 (1981). https://doi.org/10.1029/GD017p0259

[48] Obaje, N. Geology and mineral resources of Nigeria Berlin: Springer, 120, 2009, 221.

[49] O. Oluyede, et al., Field occurrence, petrography, and structural characteristics of basement rocks of the northern part of Kushaka and Birnin Gwari schist belts, northwestern Nigeria, J. Natural Sci. Res., 12 (2021) 2224-3186. https://doi.org/10.7176/jnsr%2F12-12-02

[50] A. Agbor, Geology, and geochemistry of Zungeru amphibolites, north Central Nigeria, Univers. J. Geosci., 2 (2014) 116-122. https://doi.org/10.13189/ujg.2014.020402

[51] Ogezi, A. Geochemistry and Geochronology of Basement Rocks from Northwestern, Ni geria, Ph.D. Thesis, Leeds University, 1977.

[52] Ajayi, T.R. The geochemistry and origin of the amphibolites in Ife-Ilesha area, SW Nigeria, Niger Journal of Mining and Geology 17 (1980) 179–196

[53] Rahaman, M.A. Recent advances in the study of the basement complex of Nigeria. Abstract, 1st Symposium on the Precambrian Geology of Nigeria. (1981).

[54] Egbuniwe, I. Geotectonic evolution of the Maru Belt, NW Nigeria, Unpublished Ph.D. Thesis, University of Wales, Aberystwyth, 1982.

[55] Watkin, D. 30-meter SRTM elevation data downloader, 2024. http://dwtkns.com/srtm30m/

[56] Earth Explorer :United States Geological Survey,2024. https://earthexplorer.usgs.gov

[57] R. Ranganai, C. Ebinger, Aeromagnetic and Landsat TM structural interpretation for identifying regional groundwater exploration targets, south-central Zimbabwe Craton, J. Appl.Geoph., 65 (2008) 73-83. https://doi.org/10.1016/j.jappgeo.2008.05.009

[58] D. Fossi, Structural lineament mapping in a sub-tropical region using Landsat-8/SRTM data: a case study of Deng-Deng area in Eastern Cameroon, Arab. J. Geosci., 14 (2021) 2651. https://doi.org/10.1007/s12517-021-08848-9

[59] M. Mwaniki, M. Moeller, G. Schellmann, A comparison of Landsat 8 (OLI) and Landsat 7 (ETM+) in mapping geology and visualising lineaments: A case study of central region Kenya, Int. Archives Photo. Remote Sens. Spat. Inf. Sci., XL-7/W3 (2015) 897-903. https://doi.org/10.5194/isprsarchives-XL-7-W3-897-2015

[60] A. Crosta, J. Moore, Geological mapping using Landsat thematic mapper imagery in Almeria Province, South-east Spain, Int. J. Remote Sen., 10 (1989) 505-514. https://doi.org/10.1080/01431168908903888

[61] L. Q. Hung, N. Q. Dinh, O. Batelaan, V. T. Tam, D. Lagrou, Remote sensing, and GIS-based analysis of cave development in the Suoimuoi catchment (Son La-NW Vietnam), J. Cave Karst Stud., 64 (2002) 23-33.

[62] U. Mallast, et al., Derivation of groundwater flow-paths based on semi-automatic extraction of lineaments from remote sensing data, Hydrol. Earth Syst. Sci., 15 (2011) 2665-2678. https://doi.org/10.5194/hess-15-2665-2011

[63] M. Hamath, et. aaal., Mapping mafic dyke swarms, structural features, and hydrothermal alteration zones in Atar, Ahmeyim and Chami areas (Reguibat Shield, Northern Mauritania) using high-resolution aeromagnetic and gamma-ray spectrometry data, J. Afr. Earth. Sci., 163 (2020) 103749. https://doi.org/10.1016/j.jafrearsci.2019.103749

[64] I. C. Briggs, Machine contouring using minimum curvature, Geophys., 39 (1974) 39-48. https://doi.org/10.1190/1.1440410

[65] R. J. Blakely, Potential theory in gravity and magnetic applications. Cambridge university press, (1996). https://doi.org/10.1017/CBO9780511549816

[66] M. N. Nabighian, V. J. S. Grauch, R. O. Hansen, T. R. LaFehr, Y. Li, J. W. Peirce, J. D. Phillips, and M. E. Ruder, The historical development of the magnetic method in exploration. Geophys., 70 (2005) 33ND-61ND. https://doi.org/10.1190/1.2133784

[67] G. R. Cooper, D. R. Cowan, Filtering using variable order vertical derivatives. Comput. Geosci., 30 (2004) 455-459. https://doi.org/10.1016/j.cageo.2004.03.001

[68] M. N. Nabighian, The analytic signal of two-dimensional magnetic bodies with polygonal cross-section, its properties and use for automated anomaly interpretation. Geophys., 37 (1972) 507-517. https://doi.org/10.1190/1.1440276

[69] R. J. Blakely, R. W. Simpson, Approximating edges of source bodies from magnetic or gravity anomalies. Geophys., 51 (1986) 1494–1498. https://doi.org/10.1190/1.1442197

[70] W. R. Roest, J. Verhoef, M. Pilkington, Magnetic interpretation using the 3-D analytic signal. Geophys., 57 (1992) 116-125. http://dx.doi.org/10.1190/1.1443174

[71] J. B. Thurston, R. S. Smith, J. Guillion, A multi-model method for depth estimation from magnetic data, Geophys., 67 (2002) 348-663. https://doi.org/10.1190/1.1468616

[72] H. G. Miller, V. Singh, Potential field tilt-A new concept for location of potential field sources. J. Appl. Geophys., 32 (1994) 213–217. https://doi.org/10.1016/0926-9851(94)90022-1

[73] M. L. Airo, Regional interpretation of aerogeophysical data: Extracting compositional and structural features. In Airo, M. L. (Eds.), Aerogeophysics in Finland 1972–2004: Methods, System Characteristics and Applications. Geological Survey of Finland, Special Paper 39 (2005) 176-197.

[74] L. T. Pham, et. al., Determination of subsurface lineaments in the Hoang Sa islands using enhanced methods of gravity total horizontal gradient, Vietnam J. Earth Sci, 44 (2022) 395-409. https://doi.org/10.15625/2615-9783/17013

[75] S. E. Ekwok, et. al., Application of High-Precision Filters on Airborne Magnetic Data: A Case Study of the Ogoja Region, Southeast Nigeria. Minerals, 12 (2022) 1227. https://doi.org/10.3390/min12101227

[76] J. S. Ejepu, et. al., Predictive mapping of the mineral potential using geophysical and remote sensing datasets in parts of Federal Capital Territory, Abuja, north-central Nigeria. Earth Sciences, 9 (2020) 148-163. https://doi.org/10.11648/j.earth.20200905.12

[77] A. El Galladi, S. Araffa, M. Mekkawi, M. Abd-AlHai, Exploring mineralization zones using remote sensing and aeromagnetic data, West Allaqi Area, Eastern-Desert, Egypt, Egypt. J. Remote Sens. Space Sci., 25 (2022) 417-433. https://doi.org/10.1016/j.ejrs.2022.03.007

[78] O. S. Haruna,O. W. Osisanya, O. E. Agbalagba, A. I. Korode, T. A. Ibitoye, Application of aeromagnetic in determination of lineament of Hawal basement complex Northeast Nigeria. World News Nat. Sciences, 45 (2022) 58-92.

[79] E. J. Holden, J. C. Wong, P. Kovesi, D. Wedge, M. Dentith, L. Bagas, Identifying structural complexity in aeromagnetic data: An image analysis approach to greenfields gold exploration. Ore Geol. Rev., 46 (2012) 47-59. https://doi.org/10.1016/j.oregeorev.2011.11.002

[80] J. D. Phillips, Processing and interpretation of aeromagnetic data for the Santa Cruz Basin-Patagonia Mountains Area. South- central Arizona, US Geological Survey, New York (1998). https://doi.org/10.3133/ofr0298

[81] F. O. Akinluyi, et. al., Investigation of the influence of lineaments, lineament intersections and geology on groundwater yield in the basement complex terrain of Ondo State, Southwestern Nigeria, Appl. Water Sci., 8 (2018) 1-13. http://dx.doi.org/10.1007/s13201-018-0686-x

[82] B. Boadi, et. al., Analysing multi-index overlay and fuzzy logic models for lode-gold prospectivity mapping in the Ahafo Gold District – Southwestern Ghana. Ore Geol. Rev., 148 (2022) 105059. https://doi.org/10.1016/j.oregeorev.2022.105059

[83] S. O. Sanusi, J. O. Amigun, Structural and hydrothermal alteration mapping related to orogenic gold mineralization in part of Kushaka schist belt, North-central Nigeria, using airborne magnetic and gamma-ray spectrometry data, SN Appl. Sci., 2 (2020) 1-26. https://doi.org/10.1007/s42452-020-03435-1

[84] de Quadros, T. F., J. C. Koppe, A. J. Strieder, J. F. Costa, Mineral-potential mapping: a comparison of weights-of-evidence and fuzzy methods, Nat. Resour. Res., 15 (2006) 49-65. https://doi.org/10.1007/s11053-006-9010-9

[85] R. B. Shives, B. K. Charbonneau, and K. L. Ford, The detection of potassic alteration by gamma ray spectrometry recognition of alteration related to mineralization, Fourth Decennial Intern. Conf. Mineral Exploration, (Toronto, Canada), (1997) 345–353. http://dx.doi.org/10.1190/1.1444884

[86] A. S. Eshanibli, A. U. Osagie, N. A. Ismail, H. B. Ghanush, Analysis of gravity and aeromagnetic data to determine structural trend and basement depth beneath the Ajdabiya Trough in northeastern Libya. SN Appl. Sci., 3 (2021) 1-15. https://doi.org/10.1007/s42452-021-04263-7

[87] R. W. Saaty, The Analytic Hierarchy Process—What It Is and How It Is Used. Math. Modell., 9, (1987) 161-176. https://doi.org/10.1016/0270-0255(87)90473-8

[88] K. D. Goepel, Implementation of an Online Software Tool for the Analytic Hierarchy Process (AHP-OS). Int. J. Anal. Hierarchy Process, 10 (2018) 20469-20487. https://doi.org/10.13033/ijahp.v10i3.590

[89] T. L. Saaty, Fundamentals of Decision Making and Priority Theory with the Analytic Hierarchy Process. RWS Publications, Pennsylvania. (2006). https://doi.org/10.1007/978-94-015-9799-9_2

[90] L. H. Tsoukalas, R. E. Uhrig, Fuzzy and neural approaches in engineering, New York: Wiley. (1997).

[91] P. A. Burrough, R. A. McDonnell, C. D. Lloyd, Principles of Geographical Information Systems, Oxford: Oxford University Press. (1998).

[92] G. F. Bonham-Carter, Geographic Information Systems for Geoscientists: modelling with GIS (No. 13), Elsevier. (1994).

[93] W. P. Loughlin, Principal component analysis for alteration mapping. Photogramm. Eng. Remote Sens. , 57 (1991) 1163-1169.

[94] R. H. Sillitoe, Style of high Sulphidation Gold, Silver, and Copper Mineralisation in Porphyry and Epithermal Environments. Proceeding PACRIM Congress, Bali. (1999)

[95] B. L. Dickson, K. M. Scott, Interpretation of aerial gamma-ray surveys-adding the geochemical factors. AGSO J. Aust. Geol. Geophys.AGSO, 17 (1997) 187–200.

[96] J. C. Biondi, N. D. Franke, P. R. Carvalho, S. N. Villanova, Geologia do depósito de Au Cavalo Branco (Botuverá - SC), Revista Brasileira de Geociências, 37 (2007) 445-463. http://dx.doi.org/10.25249/0375-7536.2007373445463

[97] M. Hueck, M. A. Basei, N. A. Castro, Origin and evolution of the granitic intrusions in the Brusque Group of the Dom Feliciano Belt, south Brazil: petrostructural analysis and whole rock/isotope geochemistry, J. South Am. Earth Sci., 69 (2016) 131-151. https://doi.org/10.1016/j.jsames.2016.04.004

[98] T. Cudahy, Mineral mapping for exploration: an Australian journey of evolving spectral sensing technologies and industry collaboration. Geosci., 6 (2016) 52. https://doi.org/10.3390/geosciences6040052

[99] M. Traore, J. D. Wambo, C. P. Ndepete, S. Tekin, A. B. Pour, A. M. Muslim, Lithological and alteration mineral mapping for alluvial gold exploration in the southeast of Birao area, Central African Republic using Landsat-8 Operational Land Imager (OLI) data, J. Afr. Earth. Sci., 170 (2020) 103933. https://doi.org/10.1016/j.jafrearsci.2020.103933

[100] H. Shirmard, et. al., Integration of selective dimensionality reduction techniques for mineral exploration using ASTER satellite data, Remote Sens., 12 (2020) 1261. https://doi.org/10.3390/rs12081261

[101] X. Shi, N. Al-Arifi, M. Abdelkareem, F. Abdalla, Application of remote sensing and GIS techniques for exploring potential areas of hydrothermal mineralization in the central Eastern Desert of Egypt, J. Taibah Univ. Sci., 14 (2020) 1421-1432. https://doi.org/10.1080/16583655.2020.1825184

[102] C. Moreaus, J. M. Reynoult, B. Deruelle, B. Robineau, A new tectonic model for the Cameroon Line, Central Africa. Tectonophysics, 139 (1987) 317-334. https://doi.org/10.1016/0040-1951(87)90206-X

[103] A. H. Robertson, Overview of the genesis and emplacement of Mesozoic ophiolites in the Eastern Mediterranean Tethyan region, Lithos, 65 (2002) 1-67. https://doi.org/10.1016/S0024-4937(02)00160-3

[104] G. J. Jorgensen, W. Bosworth, Gravity modelling in the Central African Rift System, Sudan: Rift geometries and tectonic significance, J. Afr. Earth Sci., 8 (1989) 283-306. https://doi.org/10.1016/S0899-5362(89)80029-6